Weather Radars

Matthew R. Kumjian

1 Introduction

Weather radar is the most indispensable tool for remote sensing of clouds and precipitation. Although initially developed for military purposes of detecting aircraft and ships, radar operators almost immediately noticed its ability to detect precipitation. Since then, advancements in radar engineering, signal processing, and meteorology have improved the accuracy, resolution, and information available from weather radars. This has led to earlier warnings, fewer false alarms, and improved understanding of hazardous weather, including severe convective storms and associated hail, tornadoes, floods, and damaging winds, as well as winter storms and associated heavy snow, precipitation transitions, and disruptive mixed-phase precipitation. The added information from new weather radar technology has led to the development and refinement of precipitation classification schemes that characterize radar pixels as one of a variety of precipitation types or non-precipitation signals, or *echoes*. This provides operational meteorologists a quick estimate of the types of radar echoes present in a given scan. These improvements have also benefited hydrometeorologists by providing valuable quantitative precipitation estimates. More recently, weather radar data are being assimilated into numerical models to improve model analyses and forecasts. Many of these topics will be treated in this and other chapters in this volume.

Radar is an acronym coined in 1940 by the U.S. Navy that stands for RAdio Detection And Ranging. Radars operate by transmitting powerful radio waves, electromagnetic radiation invisible to the human eye. At any point in space or

M. R. Kumjian (✉)
Department of Meteorology and Atmospheric Science, The Pennsylvania State University, University Park, PA, USA
e-mail: kumjian@psu.edu

C. Andronache (ed.), *Remote Sensing of Clouds and Precipitation*,
Springer Remote Sensing/Photogrammetry,
https://doi.org/10.1007/978-3-319-72583-3_2

time, one can characterize these electromagnetic waves by their *frequency* (rate of oscillation given in cycles per second or Hz), *amplitude* (intensity of the oscillating electric and magnetic fields), *phase* (point in the oscillation cycle of the electric or magnetic field), and *polarization* (direction in which the electric field vector oscillates, which is orthogonal to the direction of wave propagation). These radio waves propagate through the atmosphere and can interact with cloud and precipitation particles known as *hydrometeors*, as well as other nonmeteorological particles, biota, and ground targets. When illuminated by the radar signal, these particles undergo an electromagnetic excitation, extracting some of the radar wave's energy, radiating some of it in all directions in a process called *scattering*, and dissipating some of it as thermal energy in a process called absorption. Some of this radiation may be scattered back towards the radar (*backscattering*). The amount of the transmitted wave's power lost during propagation owing to scattering and absorption is called *attenuation*.

The backscattered signal provides important information for characterizing clouds and precipitation. For example, the amplitude of the received signal can provide information about the precipitation intensity. Because electromagnetic waves propagate through the atmosphere at a known speed (the speed of light), the time between when a signal is transmitted and when the backscattered signal is received provides the distance, or *range*, to the precipitation. The measured time rate of change of the received signal phase is the Doppler shift that tells of particles' motion towards or away from the radar. Radars that transmit and/or receive electromagnetic radiation at different polarizations or frequencies can provide additional insights into the shapes, orientations, and compositions of hydrometeors. These and other radar fundamentals will be reviewed from a conceptual framework in this chapter. More thorough discussions may be found in standard radar textbooks (e.g., [20, 34, 37, 126]).

Typically, radars are characterized by the frequency (or wavelength) of radiation they transmit. The radar's operating frequency has an important control on numerous aspects of the radar's ability to remotely sense clouds and precipitation, including the effective beam width for a given antenna size, the largest Doppler velocity that can be detected, sensitivity to precipitation, how hydrometeors respond to the incident radiation, etc. For example, for a parabolic reflector like those used by many operational weather radar networks, the effective beam width θ (in degrees) for which the radiation pattern drops to half its peak power is related to the diameter of the reflector D_R and the radar wavelength λ as $\theta \approx 70^\circ\lambda/D_R$; thus, for a given antenna reflector diameter D_R, the beam width decreases with decreasing wavelength λ (increasing frequency). Alternatively, for a given radar wavelength λ, a larger reflector size leads to a smaller beam width. Further, radiation of different λ responds differently to cloud and precipitation particles. For example, smaller-λ radiation attenuates much more than longer-λ for a given amount of hydrometeors. The tradeoff between antenna reflector size (e.g., cost, portability), effective beam width (e.g., resolution), and measurement capabilities (e.g., attenuation) are important considerations in the design of weather radar systems.

Table 1 Naming conventions for different frequency bands and wavelengths

Naming convention	Nominal frequency	Nominal wavelength
LF	30–300 kHz	10–1 km
MF	0.3–3 MHz	1000–100 m
HF	3–30 MHz	100–10 m
VHF	30–300 MHz	10–1 m
UHF	300–3000 MHz	1–0.1 m
L	1–2 GHz	30–15 cm
S	2–4 GHz	15–8 cm
C	4–8 GHz	8–4 cm
X	8–12 GHz	4–2.5 cm
Ku	12–18 GHz	2.5–1.7 cm
K	18–27 GHz	1.7–1.2 cm
Ka	27–40 GHz	1.2–0.75 cm
W	75–110 GHz	4.0–2.73 mm
G	110–300 GHz	2.73–0.1 mm

Different electromagnetic radiation frequency bands are given letter names by convention, some of which were developed during World War II and intended to be confusing to enemy spies. Table 1 provides a list of these bands and their naming convention. Typically, LF through UHF bands have been used for upper atmospheric applications (e.g., [19, 54, 57, 58, 145, 167]), whereas higher-frequency radars are used for remote sensing of clouds and precipitation. Traditional weather radars can be classified into precipitation radars (S-X bands) and cloud radars (Ku-W). Recently, G-band radars also have been proposed for cloud studies [6]. Among operational radar networks, the United States National Weather Service's Weather Surveillance Radar-1988 Doppler (WSR-88D) radars operate at S band, whereas Canadian and several South American and European countries have C-band operational radar networks. Recently, some operational networks in the United States, Asia, and Europe have incorporated gap-filling X-band radars [9, 105, 108] for improved data coverage of low levels (e.g., [137]). Owing to their smaller antenna sizes, X-band radars can be transportable, making them attractive choices for mobile radars that are often used to study tornadoes and severe convective storms (e.g., [12, 13, 39, 118, 171, 174]). Higher-frequency cloud radars predominantly have been used for research purposes (e.g., [70, 73, 92–94, 107]) and spaceborne applications (e.g., [53]).

Given this volume's focus on remote sensing of clouds and precipitation, this chapter will be limited in scope to meteorological returns. The rest of the chapter proceeds as follows. Section 2 introduces electromagnetic scattering by a single particle. Section 3 extends this discussion to scattering of radiation at different polarizations by single nonspherical particles. Scattering by a population of particles and the equivalent reflectivity factor are introduced in Sect. 4. Section 5 describes the detection and ranging of weather echoes, and Sect. 6 introduces the Doppler

effect and principles of Doppler velocity estimation. Section 7 is a basic introduction to the radar system. Section 8 introduces dual-polarization radar variables and their interpretation. Section 9 is a brief survey of the numerous weather radar applications and new avenues of research. The chapter concludes with a brief summary in Sect. 10.

2 Scattering by a Single Particle

How a hydrometeor scatters incident electromagnetic radiation is a function of its size, shape, orientation, composition (e.g., ice, liquid, mixed phase), temperature, and the frequency of the illuminating radiation. The particle's physical composition, temperature, and the radar wavelength are characterized by the *dielectric constant*, or *relative permittivity* (ϵ_r), which is a complex number that quantifies a material's response to electromagnetic radiation. For weather radar frequencies, a larger "real" part of ϵ_r leads to a greater amount of backscattered energy from a given particle size/shape and a larger phase shift imparted on a wave propagating through a collection of such particles. A larger "imaginary" part indicates greater absorption in the particles. For example, at S band (the wavelength of the U.S. WSR-88D radar network), the real part of ϵ_r for liquid water is much greater than the real part of ϵ_r for ice. Thus, liquid raindrops backscatter far greater energy than equal-sized ice particles. For precipitation radars, ϵ_r is related to the complex *refractive index m* as $\epsilon_r = m^2$. The real part of the refractive index can be thought of as the ratio of the wave's phase speed in a vacuum to that in the medium. Equivalently, the wavelength of radiation decreases in the medium compared to in a vacuum. Thus, a radar wave propagating through a dielectric medium will experience a smaller phase speed (or smaller wavelength) in the medium than in the surrounding air.

Consider an arbitrarily shaped particle composed of some dielectric material. We can decompose this particle into tiny *finite scattering elements* (e.g., [16]), represented as spheres in Fig. 1a. When an incident electric field is applied to the particle (Fig. 1b), the electrostatic force on the electrons and protons in the tiny spheres induces a net *dipole moment*, which is the vector sum of the charge magnitude times the charge separation distance for each tiny sphere summed over the particle. This can be thought of as dipoles being induced in each tiny sphere, all of which are aligned with the electric field vector (Fig. 1b). If the incident electric field is oscillating (as is the case for radar waves), then these induced dipoles oscillate at the same frequency as the incident radiation. Thus, each tiny sphere behaves as a dipole oscillator, transmitting electromagnetic wavelets in all directions. The sum of these wavelets at some point far from the particle is the total scattered wave.

The particle's size compared to the wavelength is important for determining the total scattering response. Often, the *size parameter* is used to assess the relationship between particle size and wavelength: $x = 2\pi a/\lambda$ where a is the particle characteristic length (e.g., particle equivalent spherical radius). This size

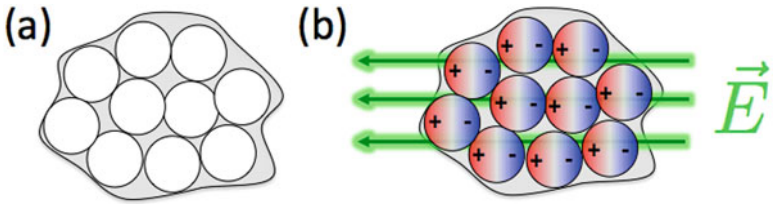

Fig. 1 (**a**) Schematic showing an arbitrary particle comprising tiny spherical finite scattering elements (white circles). (**b**) When an electric field (green vectors) is applied to the particle, a dipole moment is induced (red shading and plus signs indicate net positive charge; blue shading and minus signs indicate net negative charge), and dipoles align themselves in the direction of the electric field vector

Fig. 2 Schematic showing (**a**) a particle small compared the wavelength (traced out by the green line) in which the electric field (green vectors) is uniform throughout the particle, and (**b**) a particle large compared to the wavelength in which the electric field is nonuniform throughout the particle. In (**a**), the induced dipoles oscillate in phase with one another. In (**b**), the induced dipoles oscillate out of phase with one another

parameter can be thought of as the number of complete wave cycles of the radiation per characteristic particle length. When the particle is small compared to the wavelength of the radiation (i.e., $x \ll 1$), then there is little variation in the electric field across all the tiny spheres within the particle at some instant in time (Fig. 2a). Thus, the induced dipoles throughout the particle oscillate in phase with one another. For small spherical particles, the resulting scattered radiation pattern thus resembles that of a dipole antenna. Nonspherical particles are discussed in the following section. In contrast, for a particle large compared to the wavelength, large variations in the electric field can exist across the particle (Fig. 2b) at a given instant in time. Thus, the induced dipoles oscillate out of phase with one another, which can lead to constructive and destructive interference of the scattered wavelets. The likelihood of interference or "resonance" effects increases as the resonance parameter:

$$\Re = \frac{D\sqrt{|\epsilon_r|}}{\lambda} \tag{1}$$

approaches unity (e.g., [131]). In this expression, D is the particle's equivalent volume spherical diameter. The inclusion of relative permittivity in (1) captures the stronger scattering response (and thus greater likelihood of strong resonance effects) for particles with larger ϵ_r.

The amount of radiation scattered back towards the radar from a target is characterized by its *backscattering cross section* σ_b or *radar cross section* (traditionally,

these terms are used interchangeably in radar meteorology). Because we never know the exact scatterer characteristics at some range, we assume that the received power is from a hypothetical target that scatters radiation isotropically. The backscattering cross section is the cross-sectional area of this hypothetical isotropically scattering target. Note that the backscattering cross section often does not correspond to the actual particle's geometric area. For example, at S band, a 1-mm raindrop has a larger backscattering cross section than a 1-mm ice pellet because of the difference in relative permittivities described above.

Mie [110] provides the exact solution to σ_b of a dielectric sphere. If the spherical particles are small compared to the wavelength, the so-called Rayleigh approximation to the Mie solution for the backscattering cross section of a dielectric sphere can be employed:

$$\sigma_b \approx \frac{\pi^5}{\lambda^4} D^6 |K|^2 \tag{2}$$

where λ is the radar wavelength, and the dielectric factor K is a function of the complex refractive index m:

$$|K|^2 \equiv \left| \frac{m^2 - 1}{m^2 + 2} \right|^2 \tag{3}$$

For operational weather radars that transmit at S and C bands, many cloud and precipitation particles can be considered small compared to the wavelength. Exceptions include the largest raindrops and large melting ice particles such as hail and some snow aggregates. Additionally, many hydrometeors are not spherical, an important fact exploited by dual-polarization radars that will be discussed in Sect. 3. Approximate formulae for the backscattering cross sections of nonspherical particles are obtained by modifying the Rayleigh approximation and may be found in, e.g., [16].

3 Polarization

Recall that electromagnetic radiation's *polarization* describes the orientation direction of its electric field vector. Because electromagnetic waves are transverse waves, the polarization direction is always perpendicular to the direction of wave propagation. To understand the importance of polarization and nonspherical particles, consider again an electromagnetically small particle that comprises a large number of tiny spheres. This time, consider a hexagonal plate crystal that is aligned with its major axis approximately in the horizontal (Fig. 3). The crystal is highly nonspherical, so its response to incident radiation depends on the polarization of that radiation. Consider an illuminating horizontally polarized wave. This wave excites

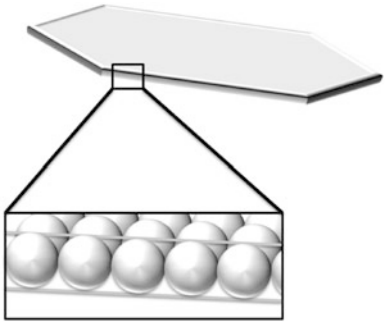

Fig. 3 Conceptual model for understanding scattering by nonspherical particles. Consider a hexagonal plate comprising a large number of tiny spheres (zoomed-in panel) that behave as dipole oscillators when illuminated with electromagnetic radiation

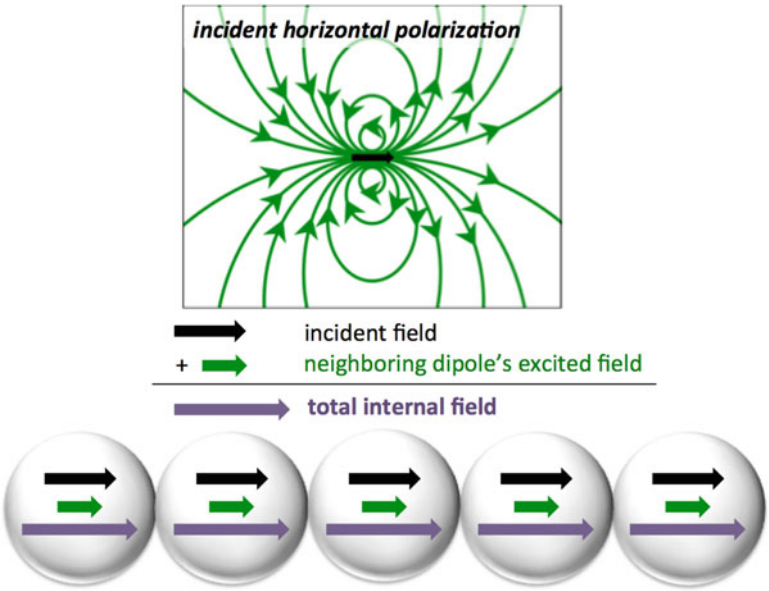

Fig. 4 Top panel: electric field lines (green) for a horizontally aligned dipole excited by an incident horizontally polarized electric field (black vector). Below: conceptual model of a horizontally oriented particle comprising a number of small spheres (cf. Fig. 3) being illuminated by an incident horizontally polarized wave (black arrow shows incident electric field). Each sphere produces a radiation pattern like the top panel. The electric field in each sphere induced by its neighbors is shown as the green vector. The resultant total internal electric field excited within each sphere is the summation of the incident and neighbors' electric fields (black+green), shown in purple. The neighboring sphere's electric field adds constructively to the incident electric field, exciting a larger total internal field. Adapted from Lu et al. [101]

the tiny spheres by inducing a dipole in each that is aligned with the electric field (in this case, horizontally). The radiation pattern from each tiny sphere is shown in Fig. 4, top panel.

Even though the induced dipoles are oscillating in phase with one another, each tiny sphere's excited field also influences its neighboring spheres (Fig. 4,

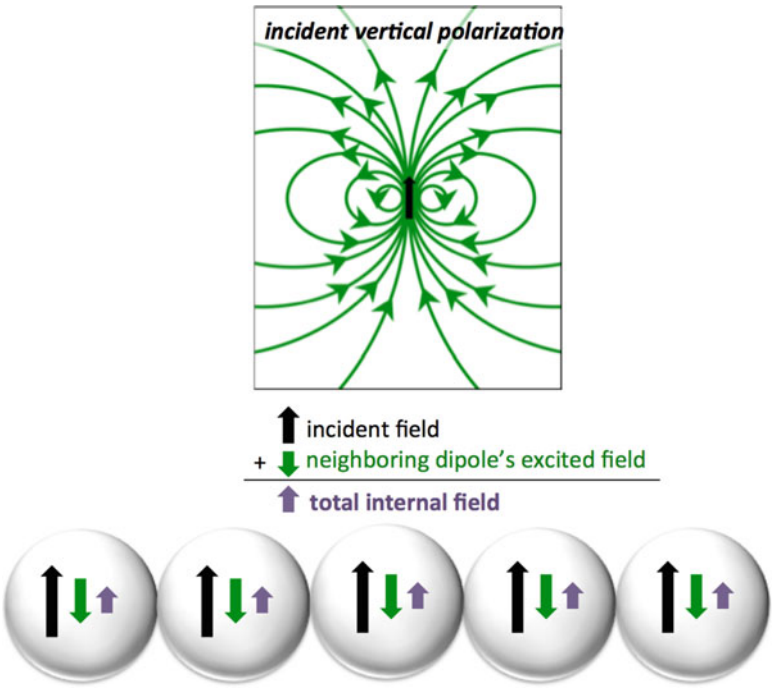

Fig. 5 As in Fig. 4, but for an incident vertically polarized wave. In this case, the neighboring spheres' electric fields (green) act in the opposite direction, and thus destructively interfere with the incident field (black). The resulting internal field (purple) is smaller in magnitude

bottom row). The electric fields from the neighbors to the immediate left and right of a given sphere (green) are in the same direction as the induced electric field within that sphere (black). Thus, these fields add constructively such that the total internal field (purple) is enhanced for a sphere with immediate neighbors to its left and right relative to that of an isolated sphere. Because the internal electric field is enhanced for such a sphere, the radiation scattered from it is also enhanced compared to an isolated sphere. Therefore, the crystal's total scattered radiation at horizontal polarization is also enhanced by these so-called *near-field interactions* (e.g., [16, 101]).

Now consider the same hexagonal crystal being illuminated by a vertically polarized wave. Again, each tiny sphere has an induced dipole, this time vertically oriented (Fig. 5, top row). However, this time the electric fields from neighbors to the immediate left and right of a given sphere (Fig. 5, bottom row, green) point in the opposite direction to the incident field (black). This leads to destructive interference, resulting in a total internal field (purple) reduced for a sphere with neighbors relative to an isolated sphere. Thus, the radiation scattered by such a sphere is reduced. Therefore, the near-field interactions reduce the crystal's total scattered radiation at vertical polarization.

By comparing Figs. 4 and 5, we see that the incident horizontally polarized wave excites a stronger internal electric field in the crystal compared to the vertically polarized wave, and thus the scattered wave from the hexagonal crystal has a larger amplitude at horizontal polarization than at vertical polarization. This is the principle behind radar polarimetry: nonspherical particles will scatter radiation differently at different polarizations, and this information may be exploited to better characterize clouds and precipitation.

Consider a hydrometeor oriented in such a way that its major axis no longer aligns perfectly with the direction of incident polarization (Fig. 6). For incident

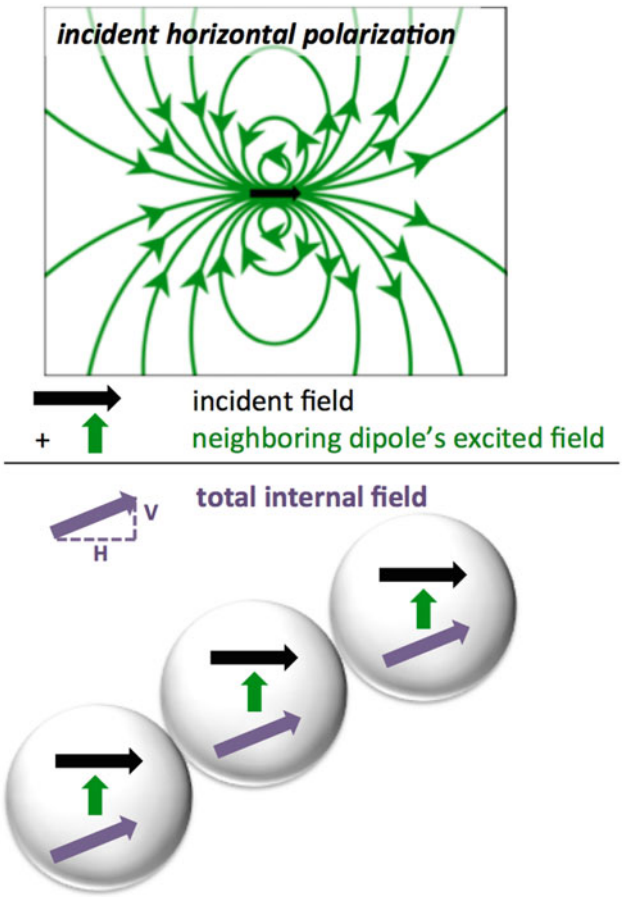

Fig. 6 As in Figs. 4 and 5, but for an incident horizontally polarized wave and a particle aligned at an angle with respect to the incident polarization direction. In this case, the electric field from neighboring spheres has a component orthogonal to the incident wave polarization direction. The resulting total internal field thus has components at both horizontal and vertical polarizations. The backscattered wave thus has components at both H and V polarizations, despite the incident wave being only horizontally polarized

horizontal polarization, each tiny sphere has an induced dipole radiation pattern with horizontal polarization, as before. This time, however, the spheres are oriented in such a way that they experience an electric field from their neighbors that has a vertical component. The total internal electric field excited in each sphere thus has components in both horizontal and vertical directions (dashed purple lines in Fig. 6). As a result, the scattered wave now has components that are both horizontally and vertically polarized, despite the incident wave being only horizontally polarized. This process, in which the particle changes the polarization of the radiation upon scattering, is known as *depolarization*. Some weather radars transmit radiation at one polarization and receive radiation at two orthogonal polarizations in order to measure the amount of depolarization that occurs in clouds and precipitation. This, too, can be used to characterize the physical properties of cloud and precipitation particles and will be discussed in Sect. 8.

4 Distributed Targets

In the atmosphere, hydrometeors typically are not isolated, single scatterers. Rather, they are found in large populations distributed within and around clouds. Therefore, when a radar wave intercepts such a population, it illuminates many particles simultaneously. The region of the atmosphere being probed by the radar at a given moment is called the *radar sampling volume*. The physical dimensions of the sampling volume are defined by the beam width (both in azimuth and elevation), and for radars that transmit pulses, the pulse length in the radial direction. Each particle in this sampling volume scatters radiation, and the total backscattered signal is the sum of the waves produced by each particle. The sum of backscattering cross sections per unit volume is called the *radar reflectivity*, η:

$$\eta \equiv \int_0^\infty \sigma_b(D) N(D)\, dD \tag{4}$$

where $N(D)dD$ is the number concentration of particles of equivalent spherical diameters D to $D + dD$ in the sampling volume. Thus, where the Rayleigh approximation is valid, we can write

$$\eta \approx \frac{\pi^5}{\lambda^4} |K|^2 Z \tag{5}$$

where we have defined the *radar reflectivity factor* (Z) as

$$Z \equiv \int_0^\infty N(D) D^6\, dD \tag{6}$$

Of course, these expressions are only useful in practice if the properties of the targets are known ahead of time. Generally, the dielectric properties of the targets (expressed through K) in the sampling volume are unknown. Further, it is generally unknown if the Rayleigh approximation is valid. Because of these uncertainties, another quantity is defined: the *equivalent radar reflectivity factor* (Z_e), which assumes a priori that the scatterers comprise small, spherical liquid drops whose backscattering cross sections can be described by the Rayleigh approximation. Thus,

$$\eta \approx \frac{\pi^5}{\lambda^4} |K_w|^2 Z_e \tag{7}$$

where the dielectric factor of liquid water K_w is used. For typical operational weather radar wavelengths, $|K_w|^2 = 0.93$. Note that $Z = Z_e$ only in the case where targets are small liquid drops. It is Z_e that is shown in operational weather radar displays, typically in base-10 logarithmic scale in units of decibels, or dBz:

$$Z_e[\text{dBz}] = 10 \log_{10} \left[\frac{Z_e[\text{mm}^6\,\text{m}^{-3}]}{1\,\text{mm}^6\,\text{m}^{-3}} \right] \tag{8}$$

This logarithmic scale is used because Z_e values can span many orders of magnitude in clouds and precipitation, from $<10^{-2}$ mm^6 m^{-3} (<-20 dBz) in non-precipitating clouds to $>10^7$ mm^6 m^{-3} (>70 dBz) in hail-bearing severe convective storms.

Each particle's scattered wavelets can constructively or destructively interfere with those from other particles in the sampling volume. This results in fluctuating received signal power as the particles "reshuffle" their relative positions within the sampling volume as they fall or move with the air flow. Thus, multiple samples are needed to estimate the mean Z_e, with sufficient time between each sample such that the samples are statistically independent. For operational weather radars under normal atmospheric conditions, this time needed for sufficient resampling and sample independence is on the order of $\leq$0.01 s. Typically, on the order of 10^1 or 10^2 samples are used to obtain a good estimate of Z_e. This combination of an adequate number of samples and the time it takes the samples to become independent through reshuffling governs the *dwell time* required for a radar to sample a particular region of the atmosphere, and thus limits the temporal resolution of the scanning. However, some research radars employ advanced techniques to mitigate this issue, allowing for faster sampling. This includes transmitting pulses of slightly different frequencies that provide independent samples in a shorter amount of time in a technique sometimes called *frequency hopping* (e.g., [13, 34, 44, 55, 56, 118]). Other radars use multiple frequencies to generate multiple, nearly simultaneous beams at different fixed elevation angles (e.g., [172]), allowing the radar to scan a larger portion of the atmosphere at once. Still others use advanced signal post-processing techniques such as *digital beam forming* (e.g., [64]) to image a large region of the atmosphere instantaneously. These advancements have substantially improved the ability of weather radars to rapidly sample hazardous storms.

Despite being one of the most often-used and familiar quantities, Z_e is challenging to calibrate to the accuracy necessary for its quantitative use. For example, most operational weather radar networks require absolute Z_e calibration to within 1 dB for acceptable errors in quantitative precipitation estimation (e.g., [47, 130]). Atlas [4] summarizes numerous techniques used for absolute radar calibration. These include using targets of known backscattering cross sections like corner reflectors or spheres suspended from balloons or aircraft, and comparisons with ground-based disdrometer measurements. Additionally, self-consistency amongst the dual-polarization radar variables in rain has been exploited for absolute radar calibration [45–47, 63, 130]. In practice, there is no clear consensus yet on the optimal calibration method.

5 Detection and Ranging of Weather Echoes

For a radar to detect a cloud or precipitation echo at a given range, the received signal must be strong enough to discern from noise. The power received from a target depends on properties of the wave propagation path to the target and back, characteristics of the radar system such as the antenna, and the properties of the target itself. These are collectively described by the so-called *radar equation*; different forms of the radar equation and derivations thereof may be found in standard radar texts (e.g., [7, 20, 34, 37, 126]). The radar equation is important because it allows the equivalent reflectivity factor Z_e to be estimated from the returned power. For example, one may increase the strength of the returned signal by increasing the radar's transmitted power, increasing the duration of the transmitted pulse, and/or increasing the size of the antenna reflector (which helps focus the transmitted beam and collect the received signal). Alternatively, more power is received if the targets scatter more radiation back to the radar and/or they are located closer to the radar, because radiation intensity decreases as $1/r^2$, where r is the distance from the source of the radiation.

Many modern weather radars are pulsed-Doppler radar systems that typically transmit 10^2–10^3 pulses per second. The amount of time a pulse lasts is the *pulse length*, which is typically on the order of a microsecond. This results in a *pulse width* on order of a few hundred meters. The rate at which these pulses are transmitted is called the *pulse repetition frequency* (PRF), which can be inverted to obtain the *pulse repetition time* (PRT), or time between consecutive pulses. The transmitted waves propagate through the atmosphere at the speed of light c. The distance to a target, or its *range* (r), thus can be determined by the time Δt it takes for a pulse to travel out and return to the radar:

$$r = \frac{c\Delta t}{2} \tag{9}$$

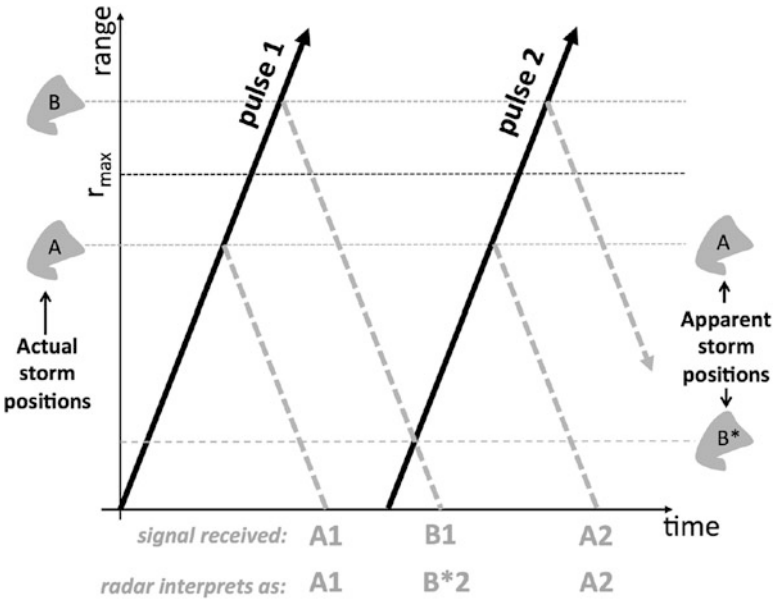

Fig. 7 Conceptual model of range aliasing. The radar fires pulse 1 (slanted black arrow) at the initial time. There are two storms, A and B, located at positions shown to the left of the graph. The maximum unambiguous range (r_{max}) is shown as the dotted black line. The backscattered signals from storms A and B are shown as dashed gray lines. The top row below the graph shows the times when these backscattered signals are actually received, where "A1" stands for the signal from storm A from pulse 1, etc. However, because storm B is located beyond r_{max}, the radar interprets its echo as coming from an apparent storm B* at a much closer range (equivalent to the actual range of storm B minus r_{max}) from pulse 2. Thus, storm B's range is said to be "aliased" or "folded"

The factor of two is because the pulse must travel out to the target and back. The fact that the radar transmits pulses every PRT limits the maximum range to which the pulse can travel to and back from before the next pulse is transmitted: $r_{\max} = c \times \mathrm{PRT}/2$. If a target is located beyond $r_{\max}$, then the signal scattered from that target is received after the next pulse has been transmitted. In this case, the radar interprets the echo as coming from the target scattering the second transmitted pulse. As a result, the target's true range is *aliased* or *folded* and incorrectly indicated as being from a range between 0 and $r_{\max}$ (Fig. 7). Modern weather radars employ more sophisticated techniques to mitigate this so-called range ambiguity (e.g., [10, 159, 160]).

Many weather radars operate in surveillance scanning modes in which the radar antenna is set at a fixed elevation and rotated in azimuth. Typically, the data are displayed from a "bird's eye" view in what has been historically called a *plan position indicator* or PPI. More modern terms synonymous with PPI include *sweep* and *surveillance scan*. Radar pixel locations in such a surveillance scan are specified by range and azimuth coordinates, which are sometimes interpolated onto a Cartesian grid (Fig. 8a). Operational scanning strategies typically comprise several

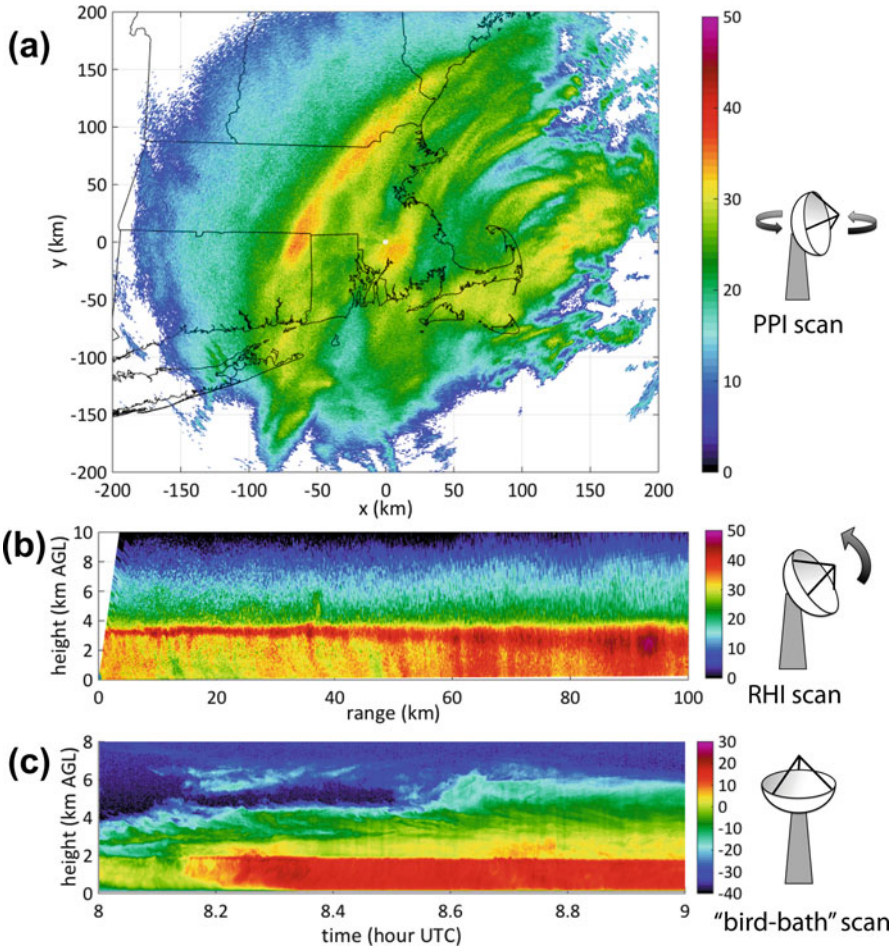

Fig. 8 Example displays from various types of radar scans with a cartoon showing the antenna scanning strategy to the right of each panel. (**a**) A PPI or surveillance scan of equivalent reflectivity factor at horizontal polarization (Z_H, in dBz, shaded according to scale) in which the radar antenna is at fixed elevation angle and varies in azimuth; the radar is located at the origin of the coordinate system. (**b**) A RHI scan of Z_H (in dBz, shaded according to scale) in which the radar antenna is at fixed azimuth and varies in elevation. (**c**) A zenith-pointing or "bird-bath" scan of Z_e (in dBz, shaded according to scale) in which the radar antenna is pointing vertically. Sometimes, the antenna is rotated in azimuth while vertically pointing

such surveillance scans at different elevation angles in collectively what is known as a *volume coverage pattern* or VCP. For example, a typical VCP employed by the U.S. National Weather Service for precipitation surveillance includes 10–15 elevation angles between 0.5° and 19.5°. Data from a VCP can be interpolated onto a single altitude for displays in what is known as a *constant-altitude plan-position indicator* (CAPPI).

If azimuth angle is held constant while the radar antenna scans in elevation, the radar can collect data from a vertical cross section through clouds and precipitation known as a *range-height indicator* (RHI) scan (Fig. 8b) in which radar pixel locations are specified by range and height. Other radars point vertically and sample clouds and precipitation as they move over the radar location. The resulting data are displayed in time-height plots (Fig. 8c). Such zenith-pointing radars may have an immobile antenna, or it may rotate in azimuth while pointing vertically. The latter is often done for calibration purposes. Because the zenith-pointing parabolic reflector antenna resembles a bowl or bird bath, such scans are colloquially referred to as "bird-bath" scans. Radar meteorologists may obtain different views of clouds and precipitation by combining one or more of these types of scans into a scanning strategy.

6 Doppler Effect

Anyone who has witnessed a passing train blowing its whistle or a passing ambulance blaring its siren has experienced the Doppler effect: the tone of the whistle or siren changes as its source moves towards or away from you. The changing tone indicates the sound waves changing frequency: an increase in frequency for sources moving towards the observer, and a decrease in frequency for sources moving away from the observer.

To understand the Doppler effect in terms of electromagnetic wave scattering, a conceptual model following [34] is presented here. Consider a stationary insect that is about to be irradiated by a transmitted pulse at a time t_0 (Fig. 9a, left). At some brief instant later ($t_0 + \delta t$; Fig. 9, right), the bug has been illuminated by some number of electromagnetic wave cycles (in the cartoon, it is 2). This time-varying electromagnetic field forces polar molecules in the bug to vibrate at the same frequency, scattering radiation at the same frequency back towards the radar. In this case, there is no Doppler shift.

Now consider a bug flying towards the radar (Fig. 9b, left). Relative to a stationary bug, the bug flying towards the radar "experiences" more rapid oscillations of the electromagnetic field: the cartoon shows the bug having experienced three complete cycles (Fig. 9b, right) in the same time period δt. More cycles over a given amount of time means a higher frequency. Because the bug has been irradiated by more cycles per second, its molecules are forced to vibrate at this higher frequency and thus scatter radiation at the higher frequency back towards the radar. This frequency shift is determined by how far the target moves in a given amount of time, or its radial speed v_r, relative to the distance over which the radar wave completes one cycle, or its wavelength λ. The Doppler frequency shift is therefore $f_D = 2v_r/\lambda$, with the factor of two arising from (1) the bug approaching the radar experiences more cycles per second of the transmitted wave, and (2) in the reference frame of the moving bug, the radar is approaching the bug at v_r and thus "experiences" more cycles per second of the scattered wave. Thus, the scattered signal has its frequency

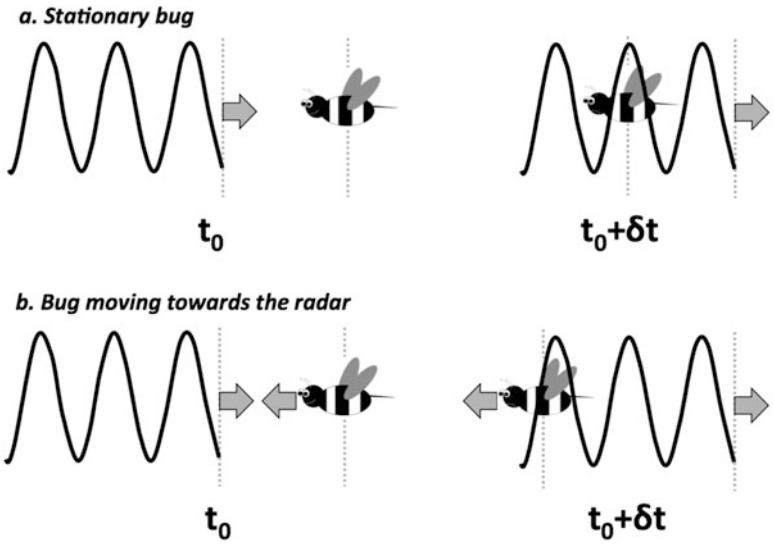

Fig. 9 Schematic explaining the physical mechanism behind the Doppler shift in the context of electromagnetic scattering. Two times are shown: t_0 (left column) and an instant later $t_0 + \delta t$ (right column). In (**a**), the bug is stationary as the wave propagates towards and irradiates it. In (**b**), the bug is traveling towards the propagating wave

shifted relative to the transmitted wave. *This is the Doppler shift*. Targets moving towards the radar produce a frequency increase, whereas targets moving away from the radar produce a frequency decrease.

Because of this frequency shift, the Doppler-shifted scattered wave will be out of sync with the transmitted wave at a given point. Thus, the Doppler-shifted wave will accumulate a phase shift (relative to the transmitted wave) at a rate of $2\pi f_D$ radians per second. By tracking phase shift over time, the radar can in principle estimate the Doppler frequency shift. In practice, however, the Doppler shift for weather applications is too small to be measured over the duration of a single pulse. For example, consider an atmospheric target moving with $v_r = 10\,\mathrm{m\,s^{-1}}$. With a 10-cm-wavelength (S-band) radar, the Doppler frequency shift $f_D = 200\,\mathrm{Hz}$. Over the duration of a typical 1-μs pulse, the resulting phase shift is only 0.072°. Thus, the phase shift is instead measured from pulse to pulse, or every PRT. For many modern weather radars, the PRT is on the order of 10^{-3} s, a much longer amount of time that allows the target to move a distance that causes a measurable phase shift.

But, just as there is a limit to the maximum range at which a radar can detect clouds and precipitation, there is a maximum radial velocity that can be detected between pulses, known as the *Nyquist velocity*. If the target moves towards the radar a distance spanning half a wavelength between pulses, then the radar cannot distinguish this from if a target moves away from the radar a distance spanning half a wavelength. In other words, the maximum velocity a radar can detect within consecutive pulses is equivalent to that which creates a phase shift of $\pm 180°$. This

Fig. 10 Schematic illustrating Doppler velocity aliasing. If the true radial velocity (gray line) exceeds the magnitude of the Nyquist velocity ($\pm v_{max}$), then the radar interprets the apparent radial velocity (dashed gray line). Note that in this case the aliased Doppler velocity is of opposite sign to the actual radial velocity

so-called *maximum unambiguous velocity* is given as $v_{\max} = \pm\lambda/(4 \times \mathrm{PRT})$. Either sign is possible given that Doppler velocity can be positive or negative; for weather radars, the typical convention is negative velocities for targets approaching the radar and positive velocities for targets moving away from the radar. If the true radial velocity of a target exceeds $v_{\max}$ in magnitude, its apparent velocity is aliased (Fig. 10).

Figure 11 shows an example of aliased Doppler velocities in a tornado sampled by an X-band Doppler on Wheels radar. The image shows a clear low-Z_H eye at the center of the tornado arising from centrifuging of debris and precipitation particles. Because the particles in the tornado have speeds towards or away from the radar in excess of the Nyquist velocity (which was about $\pm 55\,\mathrm{m\,s^{-1}}$ in this case), the velocities are aliased. This is visible as the sudden change from large positive (outbound) to large negative (inbound) velocities on the tornado's northeast side, and to a lesser extent the change of large negative to large positive velocities on the southwest side.

Notice that the PRT is found in both $r_{\max}$ and $v_{\max}$ expressions: a larger PRT (indicating a longer time between pulses) leads to a larger $r_{\max}$ but a smaller $v_{\max}$. This is known as the Doppler dilemma, which can be expressed mathematically as $|v_{\max}| \times r_{\max} = c\lambda/8 = \text{constant}$. Modern radar systems use various techniques to mitigate these ambiguities, including sampling clouds and precipitation with multiple or staggered PRTs (e.g., [10, 159, 160]).

Recall that the received signal is the result of the sum of contributions from all the scatterers within the sampling volume. Given that sample volumes are typically much larger than the radar wavelength (tens to hundreds of meters versus centimeters for precipitation radars), the total signal's phase measurement at a given location or time is meaningless for weather targets. The pulse-to-pulse change in this received phase is related to the mean radial velocity of particles within the sampling volume. Note that longer-timescale changes in phase from stationary ground clutter targets can be related to changing atmospheric conditions, which affect the atmospheric index of refraction or refractivity (e.g., [14, 38]). In general, hydrometeors in the radar sampling volume may be moving at different radial velocities owing to differences in their fall speeds, wind shear across the

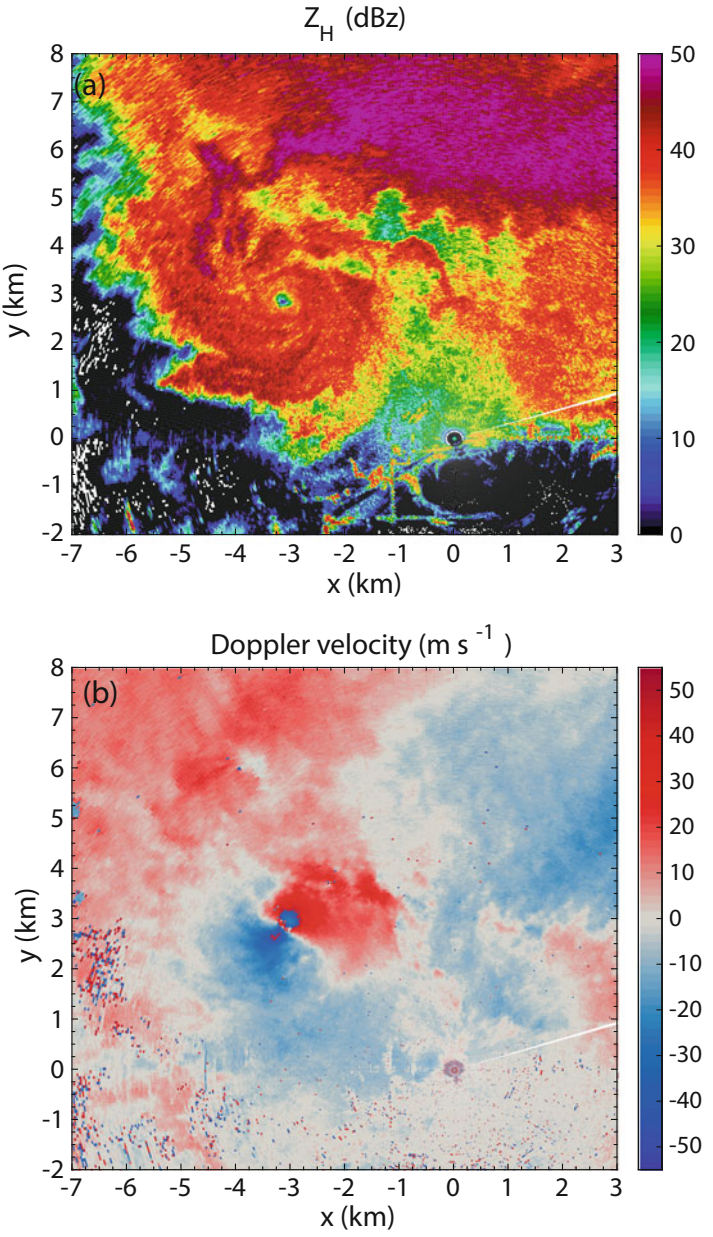

Fig. 11 Example of Doppler velocity aliasing in a tornado. Shown are surveillance scans of (**a**) Z_H (in dBz, shaded according to scale) and (**b**) Doppler velocity (in $\mathrm{m\,s^{-1}}$, shaded according to scale). Data collected on 19 May 2013 at 0045 UTC by a Doppler on Wheels X-band mobile radar, courtesy of Dr. Karen Kosiba (Center for Severe Weather Research). Positive velocities (reds) are outbound, negative (blues) are inbound. The radar is located at $x = 0\,\mathrm{km}$, $y = 0\,\mathrm{km}$, and the tornado at $x = -3\,\mathrm{km}$, $y = 3\,\mathrm{km}$

sampling volume, turbulence, etc. Because the total backscattered signal is the sum of each particle's scattered wavelet, it therefore may contain a spectrum of Doppler frequency shifts. Fourier analysis of the time series of the received signal allows for the recovery of this spectrum of frequency shifts, known as the *Doppler spectrum*.

The Doppler spectrum shows how much power scatterers contribute to the total signal as a function of their Doppler velocity. Integrating over the entire spectrum provides the total power, which is related to Z_e. The power-weighted mean value of this spectrum is the mean Doppler velocity: this is what is assigned to a given radar pixel in graphical displays. The variance of the Doppler velocities within the sampling volume is characterized by the Doppler *spectrum width*. For example, broad spectra can be associated with highly turbulent regions of storms and/or regions of enhanced wind shear, and can be useful for identifying convergent boundaries and tornadoes (e.g., [150]). Others have used Doppler spectral information to estimate turbulence and entrainment in clouds (e.g., [1, 74, 109]). Recent studies using vertically pointing cloud radars have also explored other spectral quantities such as skewness and kurtosis and their relationship to microphysical processes (e.g., [43, 75, 103, 161]).

Figure 12 shows example data collected with a vertically pointing radar during stratiform precipitation. The time-height depiction reveals a clear increase of Z_e below about 2000 m (Fig. 12a), along with an increase in magnitude of the mean Doppler velocity (Fig. 12b). This marks the transition from weaker-scattering, slower-falling snow that melts into stronger-scattering, faster-falling rain. This transition is also evident as an increase in the Doppler spectrum width (Fig. 12c), which demonstrates that raindrops have greater variance in their fall speeds than the snow and ice particles above the melting layer. The Doppler spectrum at the point given by the magenta marker is presented in Fig. 12d. It shows that most of the power is contributed by particles with Doppler velocities between about -2 and $0\,\mathrm{m\,s^{-1}}$. The dashed gray line indicates the power-weighted mean Doppler velocity ($-1.2\,\mathrm{m\,s^{-1}}$), and the gray arrows indicate two times the Doppler spectrum width ($0.5\,\mathrm{m\,s^{-1}}$). Doppler spectra can provide highly detailed information about clouds and precipitation.

7 The Radar System

Though radar technology continues to improve, many components of modern weather radars have remained fundamentally the same for several decades. Herein we describe a simplified block diagram for a pulsed Doppler radar system (Fig. 13); more technical treatments are available in standard radar engineering texts (e.g., [20, 34, 147]). The creation of the radar signal begins with the *stabilized local oscillator* (STALO), which generates a pure sinusoidal signal of frequency f_S, and the *coherent oscillator* (COHO), which generates a pure sinusoidal signal of frequency f_C that is locked in phase with the STALO signal. The COHO frequency f_C is typically much lower than the radar's operating frequency. For example, for many S-band radars

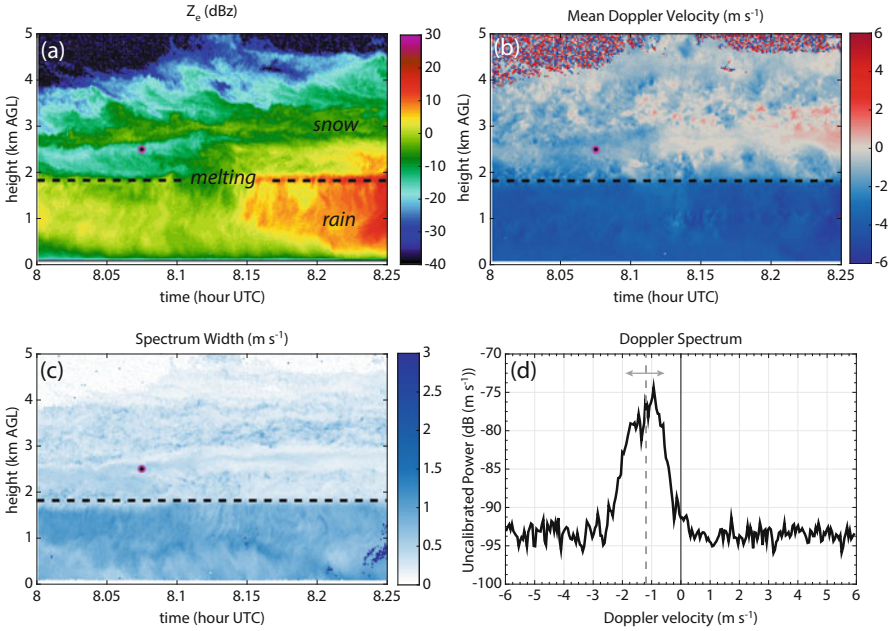

Fig. 12 Example data from the Atmospheric Radiation Measurement (ARM) Ka-band zenith-pointing radar in north-central Oklahoma, taken during a stratiform precipitation case on 27 April 2011. Shaded fields shown are time-height depictions of (**a**) equivalent reflectivity factor Z_e (dBz); (**b**) mean Doppler velocity v_r ($\mathrm{m\,s^{-1}}$); (**c**) spectrum width ($\mathrm{m\,s^{-1}}$). Panel (**d**) shows the Doppler spectrum taken at the point indicated in panels (**a**)–(**c**) as a magenta and black circle. The vertical dashed gray line shows the mean Doppler velocity ($-1.2\,\mathrm{m\,s^{-1}}$), and the double-sided arrow indicates twice the Doppler spectral width ($0.5\,\mathrm{m\,s^{-1}}$). The negative Doppler velocities indicate descending hydrometeors.

(2–4 GHz), f_C is about 30–60 MHz. This lower frequency is called the *intermediate frequency* (IF). The radar's operating frequency f_0 (sometimes called the *carrier frequency*) is usually taken to be the sum of the COHO and STALO frequencies ($f_0 = f_S + f_C$), and is obtained from mixing the COHO and STALO signals. Figure 13 indicates mixers as circled $\times$ symbols.

This continuous wave signal is modified by the *pulse modulator*, which controls the timing and width of the signal to generate a series of pulses. The pulses are then increased in intensity in the *power amplifier*. In many modern weather radars, the pulses are amplified by the *klystron*, which is essentially an electron gun that "bunches" electrons together by applying an oscillating voltage across the beam. Another power amplifier sometimes used in weather radars is the *travelling wave tube* (TWT). Historically, many radars used power oscillators known as *magnetrons*. Magnetrons are smaller and cheaper for a given output power, but generate signals with random phase. This means that the signal phase must be tracked from pulse to pulse in order to have a reference to utilize in Doppler velocity estimation. More

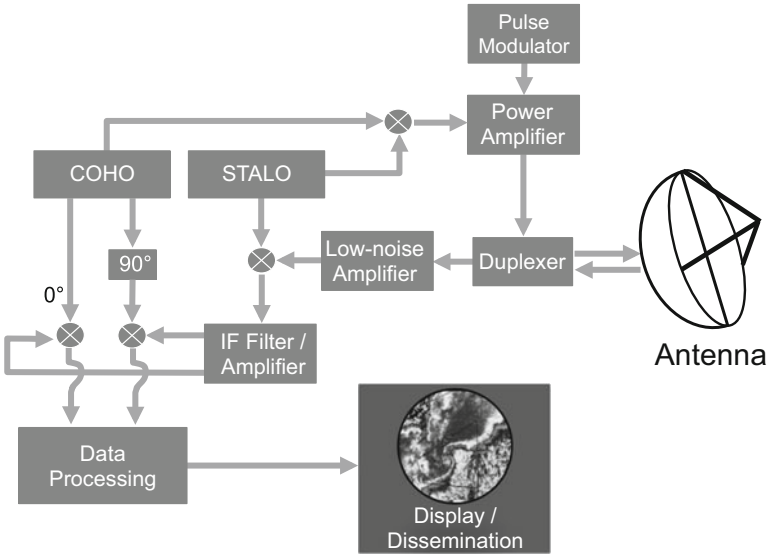

Fig. 13 Simplified block diagram showing the main components of a pulsed Doppler radar. See text for details

recently, lower-cost *solid-state transmitters* are becoming increasingly popular. Selection of transmitter type involves considering these trade-offs between power, cost, and performance.

After the pulses are amplified, they are sent to the *duplexer*. The duplexer has the important job of sending the high-power signal to the antenna during transmit times, but allowing the low-power received signal from the antenna to enter the receiving chain at other times. Sensitive electronics in the receiving chain could be severely damaged or destroyed if the high-power transmitted signal leaks into them. When transmitting, the pulsed signal is sent from the duplexer to the radar's *antenna*: the component that directs, focuses, transmits, and receives radiation. Many modern weather radars use a parabolic reflector that focuses the radiation into a narrow beam (typically, $\sim 1^\circ$ or less is desired). Radiation is sent into the parabolic reflector by the *feed horn*, which is located at the focal point of the reflector. This feed horn is typically held in place by one or more struts. Other geometries are used for cloud and precipitation radars, including the dual-offset Gregorian antenna of the CSU-CHILL radar (e.g., [69]). Recent work has focused on developing phased-array radar technology, in which an array of small microwave transmit/receive elements in a planar or cylindrical configuration is used (e.g., [176]). Such phased-array radars have the advantage of being able to direct or steer the beam electronically through phase differences applied to each of the transmitter elements, rather than needing to move the reflector to direct the radiation (e.g., [178]). However, such radars are quite expensive compared to radars employing traditional reflector antennas.

For *monostatic* radars, the same antenna that transmits radiation to the atmosphere often also serves to receive the signals backscattered from clouds, precipitation, or other targets.[1] The received signal is sent back through the duplexer, this time into the receiving chain. A principle role of the receiving chain is to amplify this signal of interest and filter out unwanted noise. Note that the received signal amplitude is often many orders of magnitude weaker than the transmitted signal, thus necessitating a *low-noise amplifier*. The received signal frequency f_R is the sum of the transmitted frequency plus any Doppler frequency shift: $f_R = f_0 \pm f_D = f_S + f_C \pm f_D$. The electronics used in weather radars work more effectively with signals of lower frequency than the one transmitted (i.e., lower than f_0). Therefore, the amplified received signal is mixed with a reference signal from the STALO in a process known as *heterodyning*. The resulting signal now is said to be *downconverted* to a frequency $f_C \pm f_D$, which is the IF plus any Doppler shift. An IF filter (sometimes called a *matched filter*) is applied to isolate this downconverted signal, which is also further amplified.

To isolate the Doppler frequency, the IF signal (with frequency $f_C \pm f_D$) is again mixed in what is often called the *phase detector*, this time with two reference signals of frequency f_C from the COHO: one at 0° phase shift with respect to the transmitted signal, and one that has been phase-shifted by 90°. Recall that identifying differences in the signal phase from pulse to pulse allows for retrieval of the Doppler velocity. Both the in-phase (0°) and quadrature (90°) signals are needed to determine whether the target is moving towards or away from the radar. These signals are then sent to the data processor, where traditional radar quantities of interest for operational and research meteorologists and hydrologists are determined. Finally, these quantities are sent for dissemination and/or display.

8 Dual-Polarization Radar Variables

Operational weather radar networks around the world have or will undergo upgrades to dual-polarization capabilities, meaning that they transmit and/or receive electromagnetic waves at two orthogonal polarizations. This is in part due to the rich information available from radars with such capabilities. More detailed reviews of the principles and applications of dual-polarization radars are available in the literature (see reviews by Zrnić and Ryzhkov [177], Kumjian [77–79] and Chandrasekar et al. [26]). Dual-polarization or "polarimetric" radars (note: "dual-polarimetric" is redundant and therefore incorrect terminology) transmit horizontally (H) and vertically (V) polarized waves, either simultaneously or alternately. In the mode of simultaneous transmission and reception (STAR) of H- and V-polarized waves, the electric field vector in general traces an ellipse in the plane perpendicular to the direction of wave propagation. Assume the amplitudes of the H- and V-polarization

[1] For bistatic radars, there are separate transmitting and receiving antennas; e.g., [170, 173].

signals are equal. If the radar's differential phase between H and V polarizations on transmit is $\pm 90°$, the electric field vector traces out a circle, and the wave is said to be *circularly polarized*. If the phase difference is $0°$ or $\pm 180°$, the electric field vector traces a line slanted between the H and V polarization directions (i.e., at $45°$ or $135°$). This is sometimes called *slant-45° linear polarization*. In the alternate transmission and reception mode, one polarization is transmitted at a time, while *both* polarizations are received. Various configurations exist for this mode: transmitting only H polarization, only V polarization, or both H and V polarizations alternately (though still one at a time). Most existing operational weather radar networks utilize STAR mode. The benefits and drawbacks of these two modes of operation are discussed in [35, 60–62, 179].

By comparing the backscattered radiation at both polarizations, one can obtain information about the shapes and types of hydrometeors present. This information is contained in the *polarimetric radar variables*, which are discussed individually in the subsections below. More comprehensive treatments are found in [20, 34, 77].

8.1 Differential Reflectivity Z_{DR}

Section 3 introduced how nonspherical particles will scatter radiation differently depending on the polarization of the illuminating radiation. Recall that Z_e is proportional to the amount of power backscattered from hydrometeors within the radar sampling volume. By comparing equivalent radar reflectivity factors at different polarizations, one can obtain information about the shape of a particle. The differential reflectivity Z_{DR} was first introduced by Seliga and Bringi [142] and is defined as the ratio of equivalent radar reflectivity factor at H polarization (Z_H) to that at V polarization (Z_V) when they are expressed in $\mathrm{mm}^6\,\mathrm{m}^{-3}$, or the difference $Z_H - Z_V$ when they are expressed in dBz. Thus, particles that scatter radiation equally at both polarizations have $Z_{\mathrm{DR}} = 0\,\mathrm{dB}$. For electromagnetically small particles, those that have more mass aligned in the horizontal have $Z_{\mathrm{DR}} > 0\,\mathrm{dB}$. Electromagnetically small particles with more mass aligned in the vertical have $Z_{\mathrm{DR}} < 0\,\mathrm{dB}$. This is because the near-field interactions between tiny finite scattering elements in the particle constructively interfere to enhance the total internal electric field at one polarization and destructively interfere to reduce the total internal electric field at the other polarization, as described in Sect. 3. For example, highly nonspherical hydrometeors like dendrites and planar crystals that tend to fall with their maximum dimensions in the horizontal can produce enormous Z_{DR} values ($>6\,\mathrm{dB}$ for extreme aspect ratios). In contrast, conical graupel particles that fall with their maximum dimension in the vertical produce negative Z_{DR} values. Raindrops become increasingly deformed by aerodynamic drag with increasing size, leading to positive Z_{DR}. For spherical particles or those that tumble randomly, radiation is equally scattered at H and V polarizations, leading to $Z_{\mathrm{DR}} = 0\,\mathrm{dB}$. For typical ranges of values at S band in different types of precipitation, see [77].

For a given particle shape, increasing the relative permittivity enhances the magnitude of the excited electric field within the particle, and thus enhances the constructive and destructive near-field interactions of tiny scattering elements, which leads to greater Z_{DR} magnitudes. For example, a nonspherical raindrop will have a larger Z_{DR} than an ice particle of identical size and shape. Particles with highly dispersed mass like fluffy snow aggregates (which in the scientific literature are sometimes characterized by a sphere or spheroidal particle with very low relative permittivity) have very weak constructive/destructive near-field interactions, and thus Z_{DR} near 0 dB. This is true even though snow aggregates tend to have highly nonspherical and irregular shapes (e.g., [67]). Aggregates also tend to have large variability in their orientation angles when falling, also leading to near-0 Z_{DR}.

If particles are electromagnetically large, resonance scattering effects obfuscate Z_{DR} interpretation, as it is no longer directly related to the particle shape. For precipitation radars, this is particularly relevant in the case of large hail. For example, calculations performed at S band (e.g., [86]) reveal negative Z_{DR} values for oriented wet, oblate hail with maximum dimension > 5 cm. Given that large hailstones tend to tumble, however, shape effects tend to be averaged out in the sampling volume, leading to observed Z_{DR} values typically near 0 dB. Z_{DR} is Z_e-weighted for a radar sampling volume filled with hydrometeors. Thus, the observed Z_{DR} is biased towards those particles that contribute the most to the overall Z_e. For populations of different particle types within a sampling volume, the observed Z_{DR} may fall somewhere between the "intrinsic" Z_{DR} of each population, depending on each population's contribution to the total Z_e.

8.2 Differential Phase Shift Φ_{DP}

As an electromagnetic wave propagates through a dielectric medium such as liquid or ice, it acquires a phase shift relative to a wave propagating the same distance in a vacuum. This is because the phase speed decreases for a wave propagating through liquid or ice (which are characterized by a refractive index greater than 1.0); equivalently, the wavelength of the radiation decreases within such a medium. Thus, the wave passing through the medium undergoes more of its 360° oscillation than a wave outside the medium at that range, leading to a phase shift relative to the freely propagating wave. This problem is often thought of conceptually as a slab of the dielectric material that extends infinitely in the directions orthogonal to the wave propagation direction but is of finite thickness in the direction of wave propagation. For this "infinite slab" model, the wave passing through the material emerges with a phase shift relative to a freely propagating wave traveling the same distance.

For particles small compared to the wavelength, one can replace the slab of the dielectric material with a slab of particles and achieve the same result (Fig. 14; see also [16]). However, the physics are different. Consider a radar pulse sampling this slab of particles. Assume the radar sampling volume extends much further radially than the radar wavelength (note that this is not shown in Fig. 14 for graphical

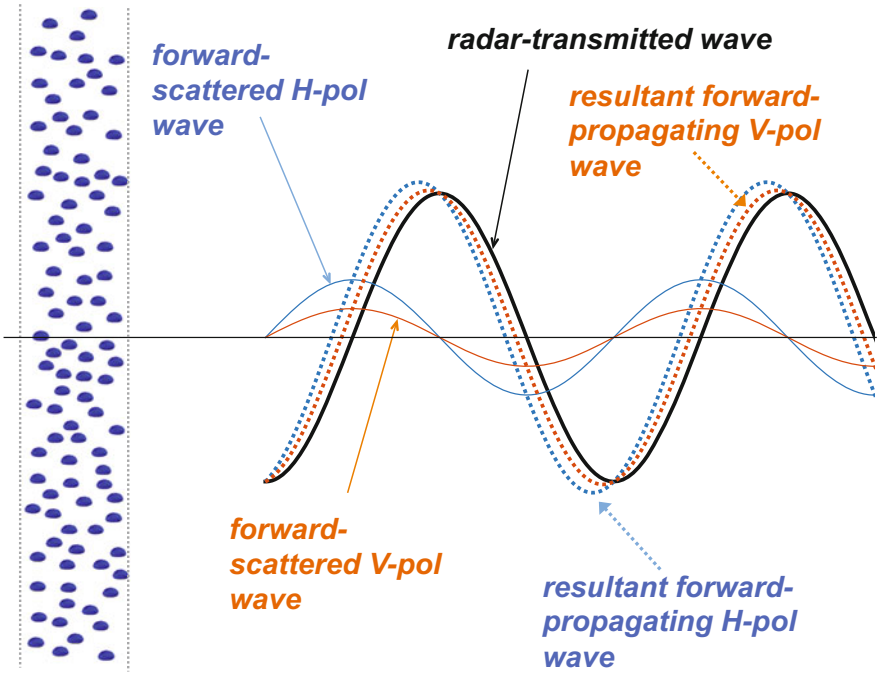

Fig. 14 Schematic showing waves propagating through an infinite slab of identical raindrops (each considered to be electromagnetically small compared to the wavelength). The solid black line is the original wave transmitted by the radar. The thin blue and orange lines represent the forward-scattered waves at H and V polarization, respectively, from the slab of raindrops, shown with a 90° phase shift. Note that the amplitude is greater for the H-polarization wave because the raindrops are oblate with their maximum dimension horizontally aligned. The total forward-propagating wave is the sum of these two, shown as the dotted lines. Note that the resultant H-polarization wave (blue dotted line) has a larger phase lag than the resultant V-polarization wave (orange dotted line); this difference is one half of Φ_{DP}. Adapted from Bohren and Huffman [16], with changes to show the polarization dependence

purposes). Thus, depending on the particles' positions within the sampling volume, dipole oscillations of particles' tiny scattering elements will be excited by different portions of the incident wave cycle. Bohren and Huffman [16] show that, for a sampling volume uniformly filled with hydrometeors, the expected mean phase shift for the forward-scattered wave at some distance beyond the slab is $90° + \Theta$ relative to the freely propagating wave, where Θ is the phase shift between the incident wave and the oscillations of the tiny scattering elements themselves. For weather radars, Θ is small and will be neglected here. In Fig. 14, the forward-scattered waves are depicted by the thin colored lines and the freely propagating incident wave is the thick black line. The total propagating wave is the sum of the phase-shifted forward-scattered waves from each of the particles illuminated in a sampling volume and the original transmitted wave (dotted colored lines in Fig. 14). The total propagation

phase shift relative to the transmitted wave propagating in free space is thus between 0° and 90°, depending on the forward-scattered wavelets' contributions. In turn, the contributions of these wavelets depend on the size and concentration of particles in the sampling volume.

For electromagnetically small particles, we expect no difference in this total propagation phase shift between H and V polarizations unless there is a difference in amplitude of these particles' forward-scattered radiation between H and V polarizations, which would contribute differently to the total propagating wave's phase shift. This will only occur if the particles are nonspherical, arising owing to the constructive/destructive near-field interactions described in Sect. 3. Note that for electromagnetically small particles, the forward- and backscattering amplitudes are identical, so the arguments applied above for backscattering are also applied to forward scattering. Therefore, for a population of horizontally aligned oblate particles like raindrops, the H-polarization forward-scattered wave provides a stronger contribution to the total forward-propagating wave than the V-polarization forward-scattered wave. Thus, the total propagation phase shift for the H-polarization wave is weighed more heavily towards this forward-scattered wave, leading to a larger phase shift than at V polarization (cf. dotted blue and orange curves in Fig. 14). This phase difference is half of the *propagation differential phase shift* Φ_{DP}; the measured Φ_{DP} comes from the two-way propagation out to the sampling volume range and back.

Seliga and Bringi [143], Jameson [65], and Sachidananda and Zrnić [136] argued for the use of Φ_{DP} for rainfall estimation. Φ_{DP} tends to increase monotonically with range for electromagnetically small horizontally aligned particles, such as raindrops at longer wavelengths. As described above, the magnitude of Φ_{DP} increases with the concentration, size, and relative permittivity of *nonspherical* particles. Unlike Z_H or Z_V, however, Φ_{DP} is not affected by the presence of spherical particles or those that scatter equally at H and V polarizations. This makes Φ_{DP} quite useful for identifying mixtures of precipitation types, such as rain mixed with hail or pristine ice crystals mixed with snow aggregates/graupel. For the latter case, Z_e may be dominated by the much larger aggregates or graupel, leading to Z_{DR} near 0 dB. However, these larger, isotropically scattering particles do not contribute much to Φ_{DP}, whereas the smaller nonspherical crystals do, leading to increasing Φ_{DP} in the presence of Z_{DR} near 0 dB (e.g., [81, 140]).

Meteorologists often use one half[2] the range derivative of Φ_{DP}, known as the *specific differential phase* K_{DP}, which provides the phase shift per unit radial distance. This allows meteorologists to more easily identify regions of heavy precipitation containing nonspherical particles, like rain. One can think of K_{DP} as a measure of the amount and/or size of nonspherical particles in the sampling volume. Because they are based on phase measurements and not power, Φ_{DP} and K_{DP} are unaffected by attenuation or differential attenuation, except in the case of total extinction of the radar signal. For this reason, these variables are often used in estimating and correcting for attenuation (e.g., [18, 22, 49, 133, 134, 148, 154]).

[2]One-half the derivative is taken because Φ_{DP} is the two-way propagation differential phase shift: out to the sampling volume and back.

In practice, the radar measures the *total differential phase shift* Ψ_{DP}, which is a combination of the propagation differential phase shift Φ_{DP}, any differential phase of the transmitted wave caused by the radar system (sometimes called the "system differential phase"), and any differential phase shift imparted on backscatter, known as the *backscatter differential phase* δ. Such backscatter differential phase generally arises from electromagnetically large, nonspherical particles. Recent studies have investigated the microphysical information content of δ in rain and melting snow (e.g., [162, 163]).

8.3 Co-polar Correlation Coefficient $\rho_{\mathbf{hv}}$

The *co-polar correlation coefficient* ρ_{hv} is the correlation between the received co-polar signals at H and V polarizations (i.e., transmitted H and received H; transmitted V and received V). It can be thought of as a measure of particle variability within the radar sampling volume, where values of 1.0 indicate perfectly homogeneous precipitation and values below 1.0 indicate particle diversity. Specifically, ρ_{hv} decreases with increasing diversity of particle shapes, orientation angles, and/or relative permittivities within the sampling volume. The simplest way to think about ρ_{hv} is as a measure of the variability of particles' intrinsic Z_{DR} within the radar sampling volume: if particles in the sampling volume have a narrow distribution of intrinsic Z_{DR} values, then ρ_{hv} is close to 1.0. When particle Z_{DR} varies dramatically within the sampling volume, ρ_{hv} is reduced. Additionally, ρ_{hv} is reduced when significant variability of differential phase shift Ψ_{DP} exists within the sampling volume. This may arise from the existence of particles producing δ in the sampling volume, or gradients of Φ_{DP} within the sampling volume (e.g., when the beam is not filled uniformly; [79, 128]). Such nonuniform beam filling is common in convective storms, resulting in radially oriented streaks of reduced ρ_{hv} extending rearward from heavy precipitation cores.

At S band, ρ_{hv} is very high (>0.98) for uniform precipitation such as pure rain or pure aggregated snow. For pristine snow crystals in the presence of aggregates, the enhanced shape diversity leads to slightly reduced ρ_{hv} (>0.95; [77]). Because of resonance scattering effects for 5–6 mm raindrops at C band, which contribute to δ, ρ_{hv} in rain at C band can fall as low as 0.93. In contrast, ρ_{hv} can be much lower (<0.85) in melting snow, melting hail, and is extremely low (<0.7) in cases of nonmeteorological scatterers like insects, birds, smoke and ash, military chaff, and tornado debris. For this reason, ρ_{hv} is often used to discriminate between precipitation and nonprecipitation echoes in operational weather radar data, and for detecting the melting layer [41, 42]. Further, it is useful in identifying ongoing tornadoes [15, 82, 129, 141, 164], as discussed in the next section.

8.4 Linear Depolarization Ratio LDR

Dual-polarization weather radars that transmit and receive H- and V-polarization signals alternately (e.g., transmit H, receive H and V; transmit V, receive H and V, etc.) can measure the amount of depolarization that occurs in precipitation. If a radar transmits radiation at H polarization, the power of the received signal at V polarization is known as the *cross-polar* power. In terms of equivalent radar reflectivity factor, this is typically written as Z_{VH} (the standard convention is that the second subscript indicates the transmitted signal polarization and the first subscript indicates the received signal polarization). The ratio of Z_{VH} to Z_H (or their difference $Z_{\mathrm{VH}} - Z_H$ if expressed in logarithmic units) is known as the *linear depolarization ratio*, or LDR. Because the cross-polar component of the backscattered signal is typically very weak, values (in dB) in most hydrometeors are negative. Radar system noise limits the lowest detectable LDR to about −40 dB. LDR is only available from radars that operate in the mode of alternate transmission and reception of H and V waves: if only H polarization is transmitted, then received V-polarization signals come from depolarization. In STAR mode, it is impossible to determine what portion of the received signal of one polarization comes from co-polar or cross-polar contributions. Thus, LDR is not available from the U.S. WSR-88D radar network, which operates in STAR mode.

LDR is enhanced when nonspherical particles have a mean orientation angle with respect to the plane of polarization. This is referred to as the *canting angle*. In most situations, hydrometeors have approximately zero mean canting angle, making LDR rather low in rain, aggregated snow, etc. However, LDR is enhanced for electromagnetically large, wobbling nonspherical particles, especially those of irregular shape like wet hail (e.g., [72]). There is also evidence that wobbling, freezing raindrops in convective storm updrafts can produced noticeably larger LDR values (e.g., [59, 87]). The melting layer "bright band" typically features locally enhanced LDR values as well (Fig. 15). Recent work has shown LDR is also useful for detecting columnar ice crystals in data collected with zenith-pointing radar [116].

9 Weather Radar Applications

The information available with dual-polarization and Doppler weather radar has led to a plethora of insights and novel applications of remote sensing data in clouds and precipitation. This section provides a limited outline of some of these applications; others will be discussed elsewhere in this volume.

Much attention has focused on detection of hazards in severe convective storms. Doppler velocity information allows operational meteorologists to identify severe winds and downbursts in convective storms (e.g., [91, 104, 125]), as well as regions of strong azimuthal shear associated with the circulations of mesocyclones and

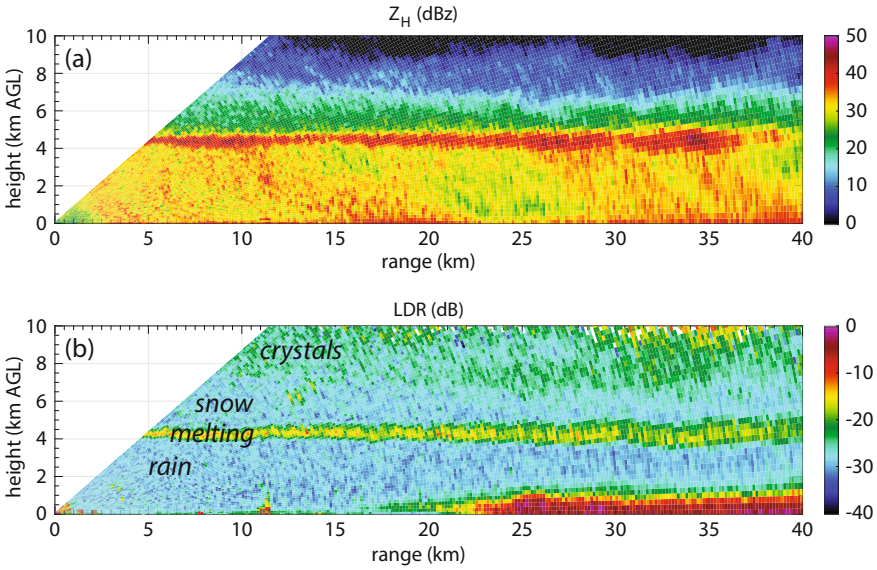

Fig. 15 Vertical cross section of (**a**) Z_H and (**b**) LDR through stratiform precipitation, collected using the SPolKa radar during a field campaign in the Indian Ocean. The melting layer bright band is clear in both Z_H and LDR. Hydrometeor types are annotated in the LDR image. LDR is enhanced in the melting layer, and slightly enhanced in a region of pristine ice crystals aloft; in snow aggregates and rain, LDR values are rather low

tornadoes (e.g., [23, 24]). Further, dynamical retrievals from weather radars have substantially improved our understanding of hazardous storms, including severe convection and tropical cyclones. When two or more Doppler radars probe the same storm from different viewing angles at approximately the same time, they measure different components of the particles' motion. In particular, they measure the radial projection of the particles' three-dimensional motion vector. The particles' horizontal motion vector usually is assumed to be equal to the horizontal wind vector, although this is a poor assumption in cases of strong vertical wind shear, or in strong circulations where centrifuging becomes important (e.g., [36, 114, 169]). With the mass continuity equation to couple horizontal and vertical motion and an estimate of particle fall speeds (typically parameterized rather crudely as a function of Z_e for scanning radars), one may estimate the three-dimensional winds. Numerous so-called *dual-Doppler* or *multiple-Doppler* synthesis techniques exist in the scientific literature (e.g., [3, 29, 40, 76, 144], among many others). These three-dimensional wind syntheses are more accurate when the radar beams sampling a particular point are separated by an angle $>30°$ and $<150°$, when both beams are at lower elevation angles, and when the radars are sampling common regions of the storm at the same time. Kinematic quantities of interest can be calculated utilizing estimates of the three-dimensional wind field obtained from multiple-Doppler syntheses to provide insights into hazardous storms. In Fig. 16, vertical

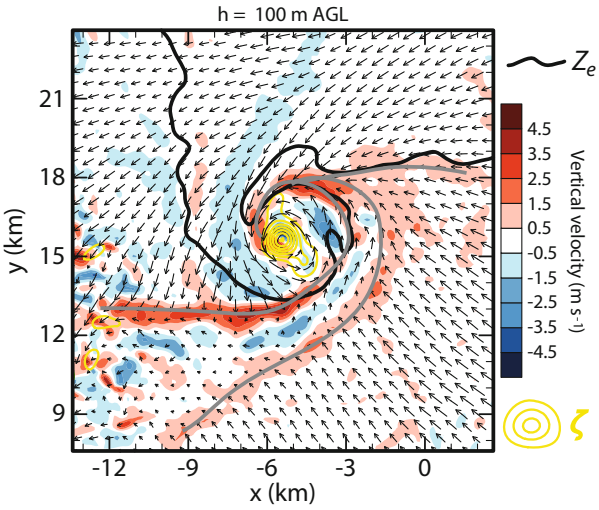

Fig. 16 Example dual-Doppler analysis showing retrieved two-dimensional horizontal wind vectors, vertical velocity (shaded in $\mathrm{m\,s^{-1}}$, according to scale), vertical vorticity (goldenrod contours), and the outline of the Z_e echo (black) at 100 m AGL. Gray lines indicate convergence lines associated with the primary and secondary rear-flank gust fronts. Image courtesy of Dr. Karen Kosiba (Center for Severe Weather Research)

velocity and vertical vorticity at 100 m AGL are shown for a tornadic supercell. Regions of updrafts and downdrafts are seen spiraling around the tornado, which is indicated by the vertical vorticity maximum.

The advent of dual-polarization radars has led to burgeoning operational algorithms aiding forecasters in hydrometeor classification (e.g., [97, 98, 117, 151, 157, 168], among many others). In these algorithms, the information content from the different radar measurements is distilled into a best-guess classification of each radar pixel into one of a set of hydrometeor or non-meteorological echo types (Fig. 17). In addition, the added information on drop sizes combined with echo classification has significantly improved quantitative precipitation estimation (QPE), although continued efforts to further refine algorithms are ongoing (e.g., [28, 41, 48, 134]). Such improvements to QPE have lead to better detection of floods (e.g., [17, 27]).

The combination of Doppler velocity information and polarimetry has allowed for improved tornado detection: strong rotation evident in Doppler velocities combined with dramatically reduced ρ_{hv} is indicative of an ongoing tornado lofting debris, as first discovered by Ryzhkov et al. [129]. The combination of irregular shapes and orientations of debris elements leads to ρ_{hv} values much lower than expected for precipitation (Fig. 18). This *tornado debris signature* has been the focus of numerous recent studies (e.g., [15, 82, 141, 164]). In some significant tornado cases, debris may be lofted to great heights and fall out on the left flank of the storm, as evident in Fig. 18. Ongoing research is exploring the utility of the tornadic debris signature for real-time information on tornado severity (e.g., [15]).

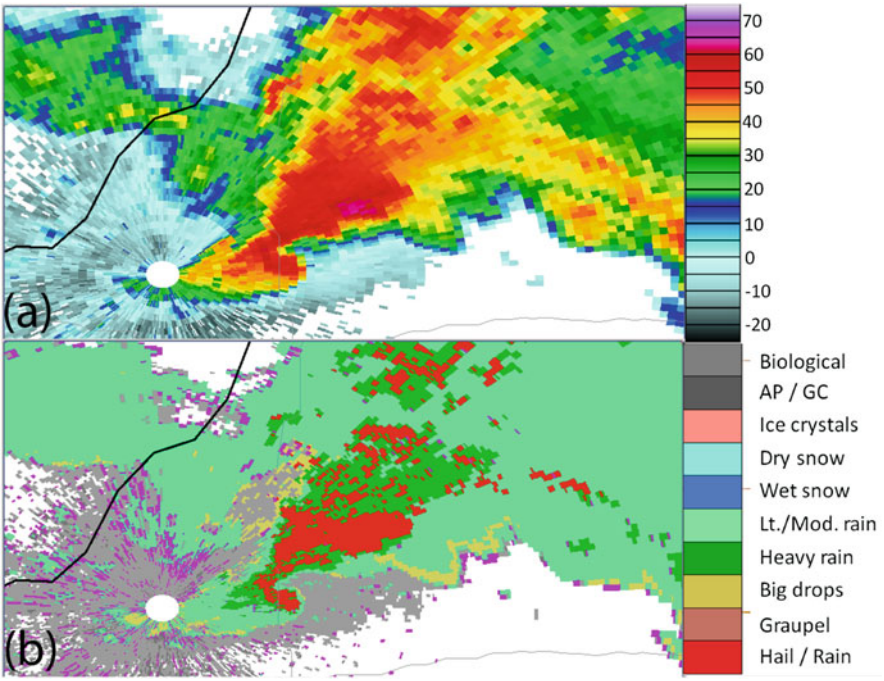

Fig. 17 Example low-level surveillance scan of (**a**) Z_H (shaded according to scale in dBz) and (**b**) output from the operational hydrometeor classification algorithm (color-coded according to scale) for a tornadic storm on 1 March 2017 in southwestern Indiana, USA, collected with the dual-polarization WSR-88D radar near Evansville (KVWX) at 0432 UTC. Magenta colors in the hydrometeor classification indicate "unknown"

The detection of damaging hail is of great interest to operational meteorologists. Dual-polarization radar can aid in hail detection owing to the differences in scattering behaviors of raindrops versus hailstones (e.g., [5, 21]). In particular, large hail tends to fall with a more chaotic orientation than raindrops, leading to Z_{DR} values near 0 dB regardless of shape. This is paired with generally large Z_H (>55 dBz), and reduced ρ_{hv} values. More recently, research efforts have focused on improving the determination of hail size [115, 132, 133]. Discrimination of small, typically non-damaging hail (<2.5 cm in diameter) from large hail is relatively straightforward with S-band dual-polarization radars (e.g., [52, 133]). This is because small hail tends to acquire a significant liquid water coating during melting [124], leading to scattering resembling large raindrops with high Z_{DR} and K_{DP} values. However, distinguishing between severe (>2.5 cm) and significantly severe (>5 cm) hail has proven challenging (e.g., [11, 115]). Some studies have suggested identifying significantly severe hail aloft, identifiable as large reductions in ρ_{hv} in the storm updraft above the environmental 0 °C level (e.g., [86, 119]), thought to arise from the presence of irregular shapes and lobes resulting from wet growth, and/or significant

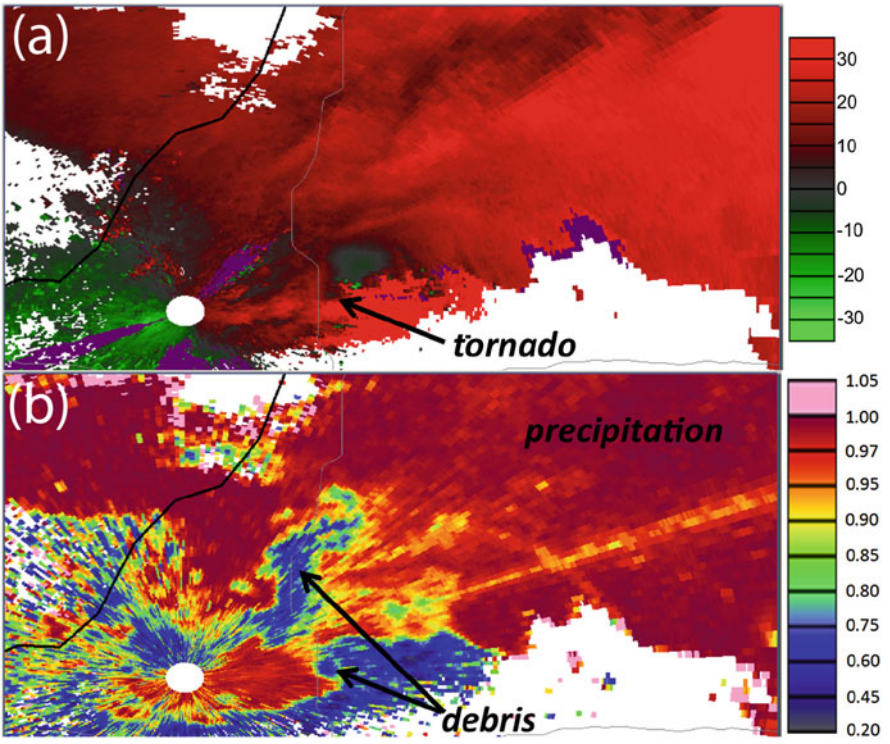

Fig. 18 As in Fig. 17, but (**a**) Doppler velocity ($\mathrm{m\,s^{-1}}$, shaded according to scale) and (**b**) ρ_{hv} (shaded according to scale) are shown. Arrows indicate the regions of Doppler-velocity-indicated rotation in (**a**) and tornadic debris as extremely low ρ_{hv} values in (**b**). The higher ρ_{hv} values indicate precipitation

resonance effects and backscatter differential phase δ. Recent work has also found anomalously high ($>10\,\mathrm{deg\,km^{-1}}$) S-band K_{DP} values in cases of extremely high concentrations of small hail that can lead to accumulations several cm deep [80]. These topics are all areas of ongoing research.

Monitoring convective storm behavior is also of interest, as weather radars can offer clues into the near-term evolution of a storm and its associated hazards. Since first discovered in the 1980s, dual-polarization radar observations of convective storms have repeatedly revealed the presence of a columnar region of positive Z_{DR} values that extends above the environmental 0 °C level (e.g., [50]), known as the Z_{DR} *column*. Figure 19 is an RHI scan through a convective storm exhibiting two Z_{DR} columns. Whereas the surrounding regions of primarily graupel and snow exhibit near-zero Z_{DR}, the positive Z_{DR} values in Z_{DR} columns indicate the updraft lofting liquid particles (raindrops or wet ice with large liquid water content) above the 0 °C level. For surveillance scans like those used by the WSR-88D radar network, Z_{DR} columns can be identified as localized enhanced Z_{DR} regions above

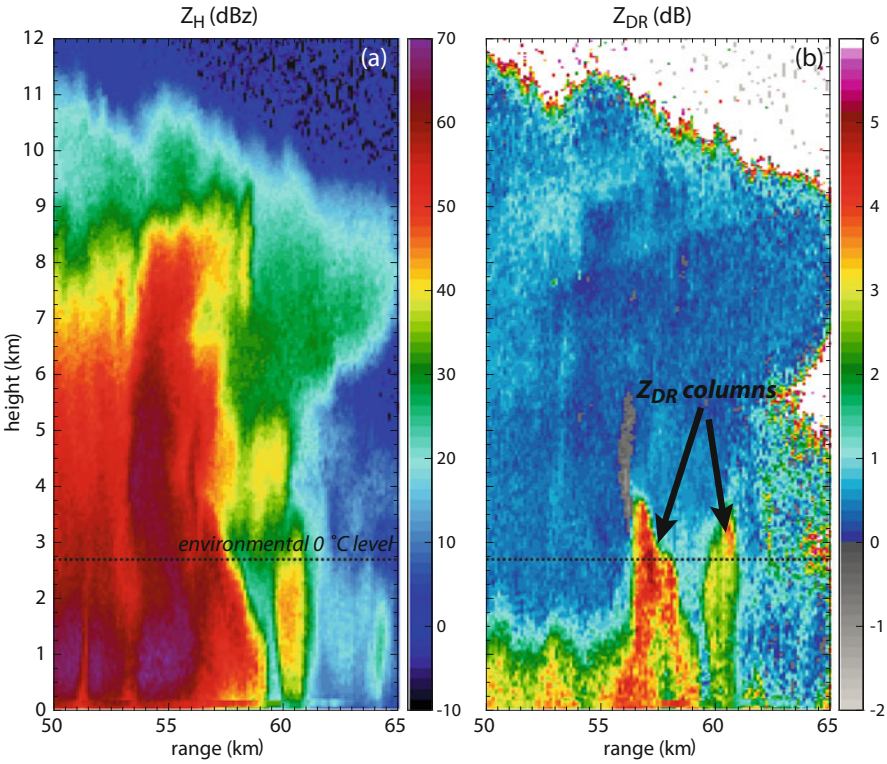

Fig. 19 Vertical cross sections of (**a**) Z_H and (**b**) Z_{DR} (shading according to scales) through a convective storm in Oklahoma on 10 February 2009. Two Z_{DR} columns are evident as positive Z_{DR} values above the environmental 0 °C level, which is annotated on both panels as the dashed line. Data from the KOUN radar in Norman, Oklahoma, courtesy of Dr. Valery Melnikov (National Severe Storms Laboratory)

the environmental 0 °C level (Fig. 20). The Z_{DR} column serves as a marker of the convective storm's updraft. In addition, the behavior of the Z_{DR} column is correlated to updraft intensity and evolution [89]. In particular, increases in the Z_{DR} column height above the 0 °C level are correlated with increases in updraft intensity, as well as subsequent increases in precipitation intensity near the surface. An operational algorithm is being developed to monitor these changes in Z_{DR} column height [149]. The breadth of the Z_{DR} column may be an important determinant of the storm's capability to produce large hail [33, 78]. Similar to Z_{DR} columns, enhanced K_{DP} columns (e.g., [59, 82, 166]) also provide diagnostic information on storm behavior and short-term evolution.

Another recent algorithm is being developed to detect regions of ongoing hydrometeor size sorting in convective storms. Such size sorting can be associated with developing convective updrafts as small drops are lofted, whereas larger, faster-falling drops and small melting ice particles are able to fall through the updraft,

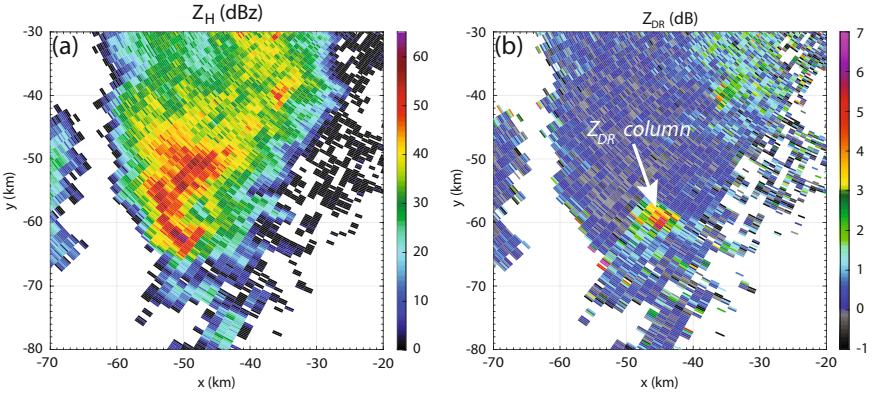

Fig. 20 Example surveillance scan at 3.2° elevation angle showing fields of (**a**) Z_H and (**b**) Z_{DR} (shading according to scales) from a severe hailstorm in southwestern South Dakota, USA. Data are from 21 June 2013, from the dual-polarization WSR-88D radar near Rapid City, SD (KUDX). The radar sampling volume at the Z_{DR} column is at a height of about 4.5 km above the radar level

resulting in large Z_{DR} values with relatively low Z_H (e.g., [84]). The Thunderstorm Risk Estimation and Nowcasting Development from Size Sorting (TRENDSS) algorithm [121] is being developed to identify such regions (Fig. 21). The algorithm works by first identifying positive Z_{DR} outliers for a given range of Z_H values in each PPI scan. These Z_{DR} anomaly data are then composited (blue shading in Fig. 21a) as a product to predict near-term convective storm trends. In Fig. 21a, areas of size sorting are detected on both the north and south flanks of the left-most cell; 20 min later, this storm has split (Fig. 21b).

Anticipating a storm's potential to produce a tornado is a key concern for operational meteorologists, as it improves the warning lead time and can save lives. A promising area of active research is in exploring the relationship between low-level dual-polarization radar signatures and the near-storm environment. In supercells and some nonsupercell tornadic storms, researchers have discovered low-level enhanced Z_{DR} and K_{DP} regions of special diagnostic value called the Z_{DR} *arc* and K_{DP} *foot*, respectively [82, 127]. The Z_{DR} enhancement region tends to be centered on a Z_H gradient, and offset from the K_{DP} enhancement region. The K_{DP} enhancement region tends to be near the storm's Z_H core in an area of heavy precipitation. This arrangement of low-level polarimetric features arises from the size sorting of hydrometeors in the presence of nonzero storm-relative flow over the lowest several km of the troposphere, which is typically associated with vertical wind shear [31, 32, 82, 83]. When the Z_{DR} enhancement region's major axis is aligned parallel to storm motion, this often implies substantial low-level storm-relative helicity (Fig. 22), an important parameter used by forecasters to assess a storm's potential to produce tornadoes (e.g., [30, 106, 123, 155, 156]). Research efforts to quantify the separation and orientation of the Z_{DR} and K_{DP} enhancement regions with respect to storm motion are ongoing (e.g., [99, 100]).

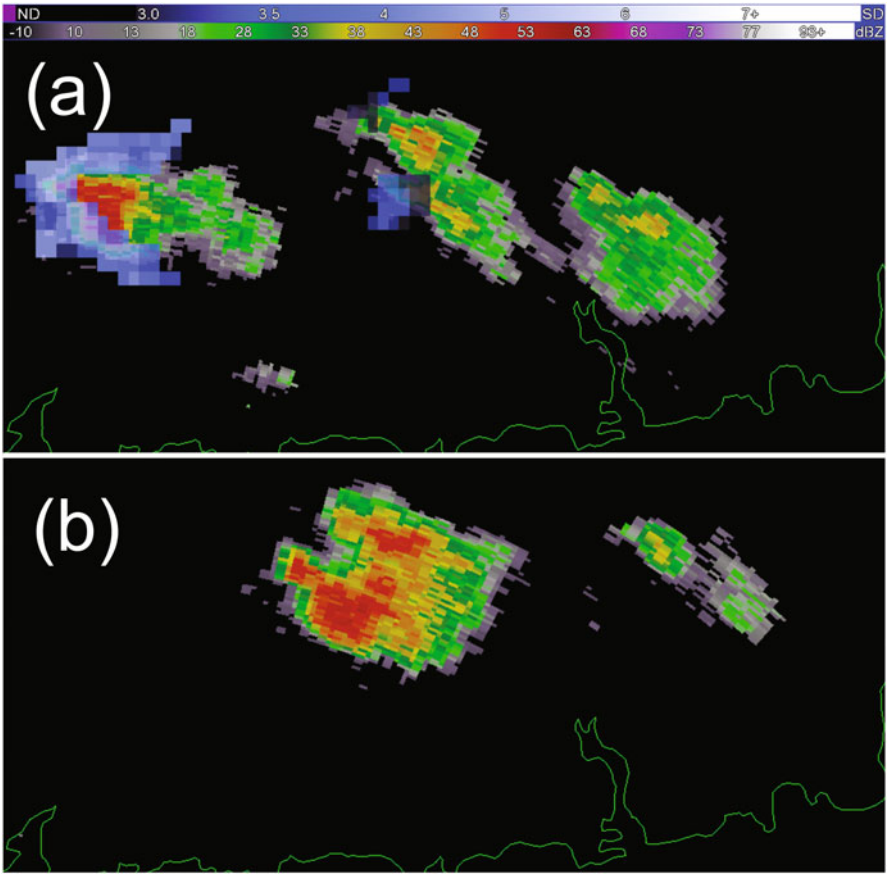

Fig. 21 Example surveillance scans of Z_H (in dBz, shaded according to scale) at two different separated by 20 min. The top panel (**a**) also includes output from the TRENDSS algorithm (blue shading), indicating areas of size sorting and potential growth on both flanks of the left-most cell. Indeed, the storm splits after 20 min (**b**). Data from multiple WSR-88D radars shown over southern Connecticut on 23 June 2015. Image courtesy of Joey Picca (Storm Prediction Center)

Polarimetric radar also provides important insights into cold-season precipitation hazards, including precipitation-type transitions and heavy snowfall. Figure 23 shows a series of surveillance scans of the ρ_{hv} field during a precipitation-type transition over Long Island, New York. Recall that a diversity of hydrometeor shapes and compositions leads to reductions in ρ_{hv}. Therefore, in mixed-phase precipitation regions when hydrometeors are melting or freezing, ρ_{hv} can be reduced. In the case shown in Fig. 23, the precipitation type reported at the Islip airport near the radar transitioned from snow to a snow/rain/ice pellets mix as the band of reduced ρ_{hv} values passed overhead (Fig. 23a, b). Once the band of reduced ρ_{hv} values moved to the north of the radar, precipitation was entirely rain (Fig. 23c, d). Operational

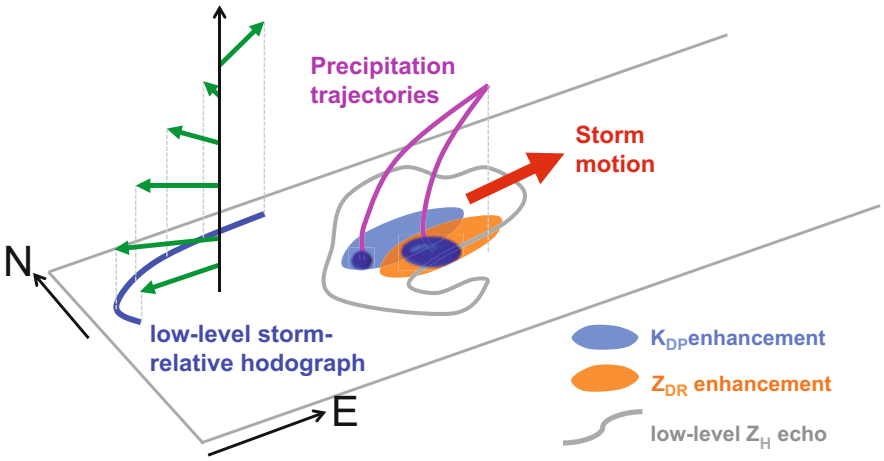

Fig. 22 Schematic showing the relationship between low-level storm-relative helicity and the offset of Z_{DR} and K_{DP} enhancement signatures at low levels. The low-level Z_H echo is shown in gray, whereas the Z_{DR} and K_{DP} enhancements are shown in orange and blue, respectively. The vertical wind profile is shown by green vectors at different altitudes, and the low-level storm-relative hodograph is shown as a thick blue curve to the left. Storm motion is indicated by the red vector. Precipitation trajectories are shown in fuchsia, indicating the fallout locations of large and small drops

forecasters make use of these important signatures from dual-polarization radar to assess precipitation transitions in real time (e.g., [120]). In addition, recent research has uncovered signatures in Z_{DR} associated with ice pellet formation and transitions from ice pellets to freezing rain [85, 88, 165]. Though this so-called *refreezing signature* has been observed in numerous cases and is a robust indicator of ice pellets, the exact underlying microphysical processes responsible for its appearance remain unknown and are a topic of current research.

Identifying regions of heavy snowfall helps forecasters monitor for locations receiving large snow accumulations. Recently, a series of studies have found that enhancements in K_{DP} at altitudes near $-15\,°C$ are associated with increased precipitation rates near the surface [2, 8, 71, 111, 138–140]. Sometimes referred to as dendritic growth zone signatures, the K_{DP} (and sometimes Z_{DR}) enhancement signifies vigorous planar crystal growth and subsequent highly efficient aggregation that together lead to heavier snowfall beneath the signatures. Depictions of such signatures in time-height format known as quasi-vertical profiles (QVPs; e.g., [135]) show a clear association between enhanced K_{DP} aloft and heavy snowfall (large Z_H) below (Fig. 24). The QVP technique was recently extended to include Doppler velocity and estimates of mesoscale divergence/convergence over the radar by Kumjian and Lombardo [81]; such depictions also show a clear connection between enhanced mesoscale ascent and vigorous planar crystal growth signatures near $-15\,°C$ (Fig. 24). In the case shown in Fig. 24, snowfall rates beneath the enhanced K_{DP} signature exceeded $15\,cm\,h^{-1}$ at times.

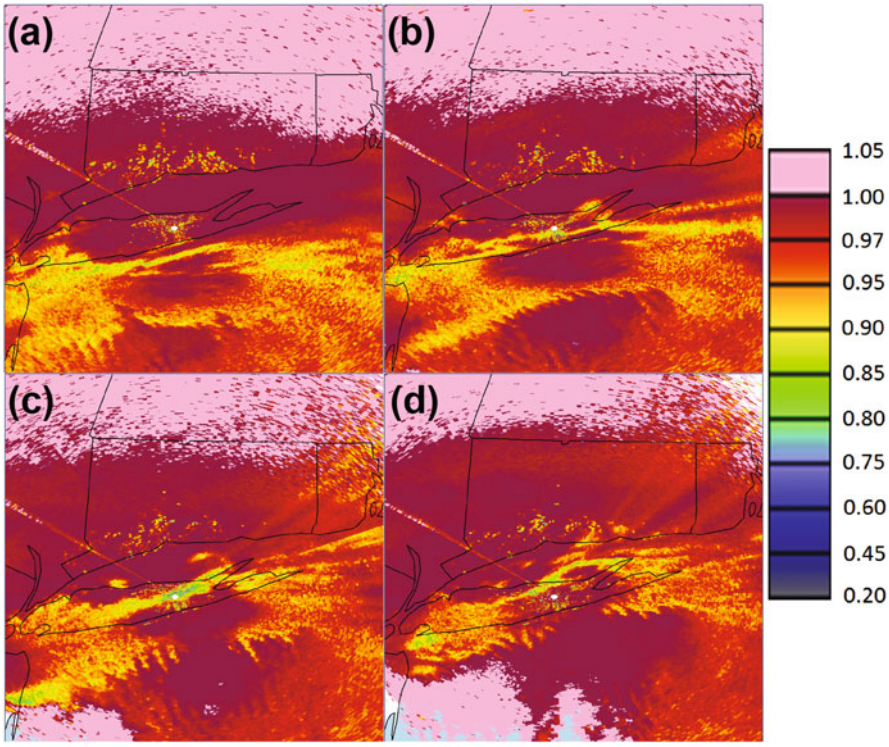

Fig. 23 Time series of 0.5° elevation angle surveillance scans of ρ_{hv} (shaded according to scale) from a winter storm precipitation transition over Long Island, New York, USA, on 13 February 2014. Data are from the dual-polarization WSR-88D radar near Upton, NY (KOKX) from (**a**) 1426 UTC, (**b**) 1456 UTC, (**c**) 1526 UTC, and (**d**) 1556 UTC

Supercooled liquid water in cold clouds can pose a serious icing hazard to aircraft. However, owing to their small sizes, cloud droplets cannot be detected in the presence of other much larger precipitation particles directly with low-frequency precipitation radars. Thus, detection of supercooled liquid water remains a significant challenge for weather radars. Instead, researchers are looking for indirect indicators of supercooled liquid water, such as the presence of ongoing riming and secondary ice production. A promising signature in dual-polarization weather radar observations may be enhanced K_{DP} collocated with near-zero Z_{DR} at temperatures between about −3 and −8 °C, which are thought to indicate the presence of quasi-spherical rimed particles (graupel) and/or aggregates with large concentrations of needle-like crystals (e.g., [43, 81, 90, 146]). Coordinated in situ measurements and polarimetric radar data are needed to verify the relationship between these signatures and the presence of supercooled liquid water.

One of the greatest challenges involving weather radar is combining advanced weather radar observations and numerical models. In particular, assimilation of

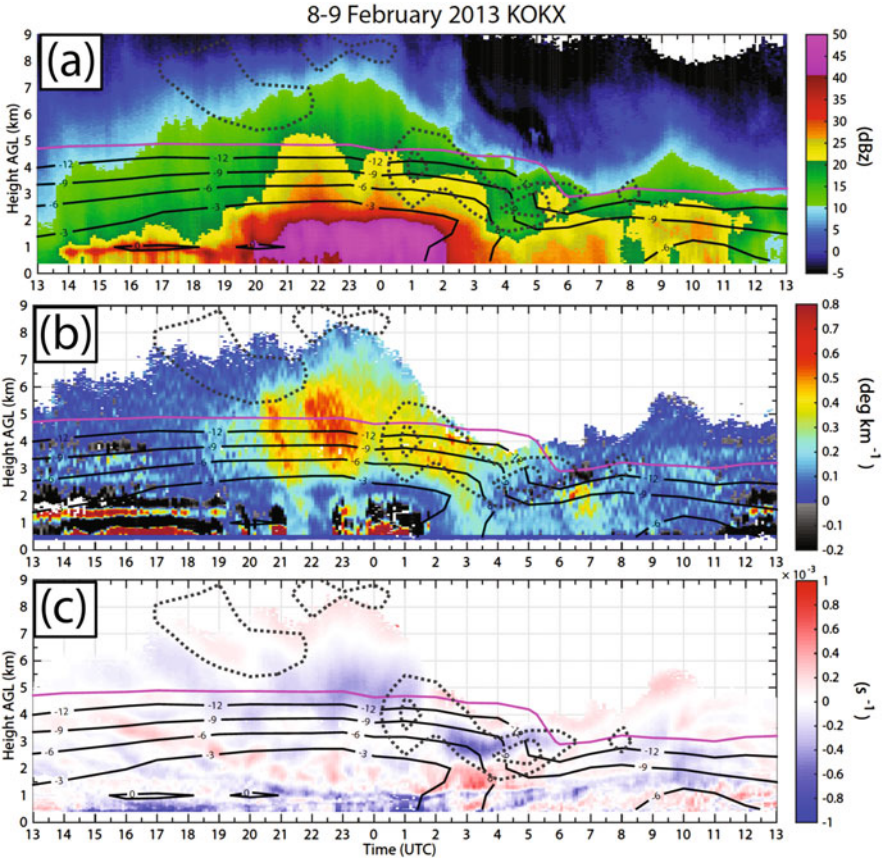

Fig. 24 Time series of quasi-vertical profiles (QVPs) of (**a**) Z_H, (**b**) K_{DP}, and (**c**) large-scale divergence during the 8–9 February 2013 blizzard, values shaded according to scales. Data from the dual-polarization WSR-88D radar near New York, NY (KOKX). Overlaid are temperature contours from the Rapid Refresh model (black curves, −12 to 0 °C in 3 °C increments, and magenta line indicating −15 °C) and mesoscale ascent (black dotted lines, starting at $-1\,\text{Pa}\,\text{s}^{-1}$ in 1-Pa s^{-1} increments). Adapted from Kumjian and Lombardo [81], with changes

dual-polarization radar data is an area of ongoing research (e.g., [68, 122, 175]). This is difficult given that many operational numerical weather prediction (NWP) models employ simplified microphysics schemes that provide no information about particle shapes, fall behaviors, or the water content in mixed-phase hydrometeors. Crucially, these particle properties exert the strongest influences on the observed radar quantities. In turn, the radar observables are strongly biased by the largest particles in the sampling volume, and exhibit a highly uncertain relationship with typical model prognostic variables like total number concentration and total mass content, which are not as sensitive to the large-size tail of the particle size distribution. Currently, many *forward operators* (the bridge between model-

predicted variables and observed radar variables) have built-in assumptions about many of these important particle properties (e.g., [68, 131]). Many current forward operators for use in radar data assimilation are overly simplistic (e.g., [95, 96, 158]), leading to large uncertainties [25]. However, recent advances in numerical modeling reveal a push towards predicting particle properties (e.g., [51, 66, 112, 113]), which may facilitate the blending of NWP models and weather radar data (e.g., [152, 153]). Future work in advanced electromagnetic scattering calculations for complex particle shapes such as snow crystals will also lead to improvements in forward operators (e.g., [102]).

10 Summary and Conclusion

This chapter highlights the fundamentals of radar remote sensing of clouds and precipitation and recent advances in hydrometeorological applications of weather radar. Radar remains the most important tool for examining clouds and precipitation. In particular, dual-polarization Doppler weather radar observations have facilitated novel insights into cloud and precipitation physics, as well as operationally important advances in the detection and monitoring hazardous weather. This includes severe convective storms (hail, tornadoes, damaging winds, floods) and winter storms (heavy snow, precipitation-type transitions). Algorithms for classification of radar echoes and quantitative precipitation estimation have also made substantial improvements in recent decades. Future breakthroughs undoubtedly will involve improvements to our understanding of fundamental physical processes in clouds and precipitation and the blending of numerical weather prediction models and polarimetric Doppler weather radar observations via data assimilation. The remainder of this volume covers many of these important applications of radar remote sensing.

Acknowledgements The author is grateful for the opportunity to contribute to this volume and thanks Dr. Constantin Andronache for facilitating the process. In addition, he would like to acknowledge the fruitful conversations and material provided by Joseph Picca (National Weather Service-Storm Prediction Center), Israel Silber (Penn State University), Marcus van Lier-Walqui (Columbia University and National Aeronautics and Space Administration Goddard Institute for Space Studies), Hughbert Morrison (National Center for Atmospheric Research), and Olivier Prat (North Carolina Institute for Climate Studies, North Carolina State University). In particular, he thanks his Penn State colleagues for numerous discussions over the last several years: Kültegin Aydin, Craig Bohren, Anthony Didlake, Eugene Clothiaux, Steven Greybush, Jerry Harrington, Paul Markowski, James Marquis, Yvette Richardson, and Johannes Verlinde. Finally, he would like to thank his awesome students in the Penn State RADAR, INC. group: Robert Schrom, Dana Tobin, Kyle Elliott, Scott Loeffler, Steven Naegele, John Banghoff, Charlotte Martinkus, and Zhiyuan Jiang. Radar data examples used in this chapter were obtained courtesy of the National Oceanic and Atmospheric Administration and the U.S. Department of Energy Atmospheric System Research program. The author would like to thank Scott Collis (Argonne National Laboratory), Karen Kosiba (Center for Severe Weather Research), and Angela Rowe (University of Washington) for their helpful critiques of this work.

References

1. Albrecht, B., M. Fang, and V. Ghate. 2016. Exploring stratocumulus cloud-top entrainment processes and parameterizations by using Doppler cloud radar observations. *Journal of the Atmospheric Sciences* 73: 729–742.
2. Andrić, J., M.R. Kumjian, D.S. Zrnić, J.M. Straka, and V.M. Melnikov. 2013. Polarimetric signatures above the melting layer in winter storms: an observational and modeling study. *Journal of Applied Meteorology and Climatology* 52: 682–700.
3. Armijo, L. 1969. A theory for the determination of wind and precipitation velocities with Doppler radars. *Journal of the Atmospheric Sciences* 26: 570–573.
4. Atlas, D. 2002. Radar calibration: Some simple approaches. *Bulletin of the American Meteorological Society* 83: 1313–1316.
5. Aydin, K., T.A. Seliga, and V. Balaji. 1986. Remote sensing of hail with a dual linear polarized radar. *Journal of Climate and Applied Meteorology*, 25: 1475–1484.
6. Battaglia, A., C.D. Westbrook, S. Kneifel, P. Kollias, N. Humpage, U. Löhnert, J. Tyynelä, and G.W. Petty. 2014. G band atmospheric radars: a new frontier in cloud physics. *Atmospheric Measurement Techniques* 7: 1527–1546.
7. Battan, L.J. 1973. *Radar Observation of the Atmosphere*, 324. Chicago: University of Chicago Press,
8. Bechini, R., L. Baldini, and V. Chandrasekar. 2013. Polarimetric radar observations of the ice region of precipitation clouds at C-band and X-band radar frequencies. *Journal of Applied Meteorology and Climatology* 52: 1147–1169.
9. Beck, J., and O. Bousquet. 2013. Using gap-filling radars in mountainous regions to complement a national radar network improvements in multiple-Doppler wind syntheses. *Journal of Applied Meteorology and Climatology* 52: 1836–1850.
10. Bharadwaj, N., and V. Chandrasekar. 2007. Phase coding for range ambiguity mitigation in dual-polarized Doppler weather radars. *Journal of Atmospheric and Oceanic Technology* 24: 1351–1363.
11. Blair, S.F., D.R. Deroche, J.M. Boustead, J.W. Leighton, B.L. Barjenbruch, and W.P. Gargan. 2011. A radar-based assessment of the detectability of giant hail. *Electronic Journal of Severe Storms Meteorology* 6 (7): 1–30.
12. Bluestein, H.B., W.P. Unruh, D.C. Dowell, T.A. Hutchinson, T.M. Crawford, A.C. Wood, and H. Stein. 1997. Doppler radar analysis of the Northfield, Texas, tornado of 25 May 1994. *Monthly Weather Review* 125: 212–230.
13. Bluestein, H.B., M.M. French, I. PopStefanija, R.T. Bluth, and J.B. Knorr. 2010. A mobile, phased-array Doppler radar for the study of severe convective storms The MWR-05XP. *Bulletin of the American Meteorological Society* 91: 579–600.
14. Bodine, D.J., D. Michaud, R.D. Palmer, P.L. Heinselman, J. Brotzge, N. Gasperoni, B.L. Cheong, M. Xue, and J. Gao. 2011. Understanding radar refractivity sources of uncertainty. *Journal of Applied Meteorology and Climatology* 50: 2543–2560.
15. Bodine, D.J., M.R. Kumjian, R.D. Palmer, P.L. Heinselman, and A.V. Ryzhkov. 2012. Tornado damage estimation using polarimetric radar. *Weather and Forecasting* 28: 139–158.
16. Bohren, C., and D. Huffman. 1983. *Absorption and Scattering of Light by Small Particles*, 530. Wiley, New York.
17. Boodoo, S., D. Hudak, A. Ryzhkov, P. Zhang, N. Donaldson, D. Sills, and J. Reid. 2015. Quantitative precipitation estimation from a C-band dual-polarized radar for the 8 July 2013 flood in Toronto, Canada. *Journal of Hydrometeorology* 16: 2027–2044.
18. Borowska, L., A.V. Ryzhkov, D.S. Zrnić, C. Simmer, and R.D. Palmer. 2011. Attenuation and differential attenuation of 5-cm-wavelength radiation in melting hail. *Journal of Applied Meteorology and Climatology* 50: 59–76.
19. Bremer, J., and U. Berger. 2002. Mesospheric temperature trends derived from ground-based LF phase-height observations at mid-latitudes comparison with model simulations. *Journal of Atmospheric and Solar - Terrestrial Physics* 64: 805–816.

20. Bringi, V., and V. Chandrasekar. 2001. *Polarimetric Doppler Weather Radar Principles and Applications*, 636. Cambridge: Cambridge University Press.
21. Bringi, V.N., J. Vivekanandan, and J.D. Tuttle. 1986. Multiparameter radar measurements in Colorado convective storms. Part II: Hail detection studies. *Journal of the Atmospheric Sciences* 43: 2564–2577.
22. Bringi, V.N., V. Chandrasekar, N. Balakrishnan, and D.S. Zrnić. 1990. An examination of propagation effects on radar measurements at microwave frequencies. *Journal of Atmospheric and Oceanic Technology* 7: 829–840.
23. Brown, R.A., L.R. Lemon, and D.W. Burgess. 1978. Tornado detection by pulsed Doppler radar. *Monthly Weather Review* 106: 29–38.
24. Burgess, D.W., L.D. Hennington, R.J. Doviak, and P.S. Ray. 1976. Multimoment Doppler display for severe storm identification. *Journal of Applied Meteorology* 15: 1302–1306.
25. Carlin, J.T., A.V. Ryzhkov, J.C. Snyder, and A.P. Khain. 2016. Hydrometeor mixing ratio retrievals for storm- scale radar data assimilation Utility of current relations and potential benefits of polarimetry. *Monthly Weather Review* 144: 2981–3001.
26. Chandrasekar, V., R. Keranen, S. Lim, and D. Moisseev. 2013. Recent advances in classification of observations from dual polarization weather radars. *Atmospheric Research* 119: 97–111.
27. Chang, W.-Y., J. Vivekanandan, K. Ikeda, and P.-L. Lin. 2016. Quantitative precipitation estimation of the epic 2013 Colorado flood event: Polarization radar-based variational scheme. *Journal of Applied Meteorology and Climatology* 55: 1477–1495.
28. Cifelli, R., V. Chandrasekar, S. Lim, P.C. Kennedy, Y. Wang, and S.A. Rutledge. 2011. A new dual-polarization radar rainfall algorithm application in Colorado precipitation events. *Journal of Atmospheric and Oceanic Technology* 28: 352–364.
29. Collis, S., A. Protat, P.T. May, and C. Williams. 2013. Statistics of storm updraft velocities from TWP-ICE including verification with profiling measurements. *Journal of Applied Meteorology and Climatology* 52: 1909–1922.
30. Davies-Jones, R., D.W. Burgess, and M. Foster. 1990. Test of helicity as a forecast parameter. In *16th Conference on Severe Local Storms*, Kananaskis Park, AB, Canada. 588–592. Boston: American Meteor Society (Preprints).
31. Dawson, D.T., E.R. Mansell, Y. Jung, L.J. Wicker, M.R. Kumjian, and M. Xue. 2014. Low-level ZDR signatures in supercell forward flanks: The role of size sorting and melting of hail. *Journal of the Atmospheric Sciences* 71: 276–299.
32. Dawson, D.T., E.R. Mansell, and M.R. Kumjian. 2015. Does wind shear cause hydrometeor size sorting? *Journal of the Atmospheric Sciences* 72: 340–348.
33. Dennis, E.J., and M.R. Kumjian. 2017. The impact of vertical wind shear on hail growth in simulated supercells. *Journal of the Atmospheric Sciences* 74: 641–663.
34. Doviak, R.J., and D.S. Zrnić. 1993. *Doppler Radar and Weather Observations*, 562. San Diego: Academic Press.
35. Doviak, R.J., V. Bringi, A. Ryzhkov, A. Zahrai, and D.S. Zrnić. 2000. Considerations for polarimetric upgrades to operational WSR-88D radars. *Journal of Atmospheric and Oceanic Technology* 17: 257–278.
36. Dowell, D.C., C.R. Alexander, J. Wurman, and L.J. Wicker. 2005. Centrifuging of hydrometeors and debris in tornadoes: radar-reflectivity patterns and wind-measurement errors. *Monthly Weather Review* 133: 1501–1524.
37. Fabry, F. 2015. *Radar Meteorology Principles and Practice*, 256. Cambridge: Cambridge University Press.
38. Fabry, F., C. Frush, I. Zawadzki, and A. Kilambi .1997. On the extraction of near-surface index of refraction using radar phase measurements from ground targets. *Journal of Atmospheric and Oceanic Technology* 14: 978–987.
39. French, M.M., D.W. Burgess, E.R. Mansell, and L.J. Wicker. 2015. Bulk hook echo raindrop sizes retrieved using mobile, polarimetric Doppler radar observations. *Journal of Applied Meteorology and Climatology* 54: 423–450.
40. Gal-Chen, T. 1978. A method for the initialization of the anelastic equations: implications for matching models with observations. *Monthly Weather Review* 106: 587–606.

41. Giangrande, S.E., and A.V. Ryzhkov. 2008. Estimation of rainfall based on the results of polarimetric echo classification. *Journal of Applied Meteorology and Climatology* 47: 2445–2462.
42. Giangrande, S.E., J.M. Krause, and A.V. Ryzhkov. 2008. Automatic designation of the melting layer with a polarimetric prototype of the WSR-88D radar. *Journal of Applied Meteorology and Climatology* 47: 1354–1364.
43. Giangrande, S.E., T. Toto, A. Bansemer, M.R. Kumjian, S. Mishra, and A.V. Ryzhkov. 2016. Insights into riming and aggregation processes as revealed by aircraft, radar, and disdrometer observations for a 27 April 2011 widespread precipitation event. *Journal of Geophysical Research-Atmospheres* 121: 5846–5863.
44. Girardin-Gondeau, J., F. Baudin, and J. Testud. 1991. Comparison of coded waveforms for an airborne meteorological Doppler radar. *Journal of Atmospheric and Oceanic Technology* 8: 234–246.
45. Goddard, J.W.F., J. Tan, and M. Thurai. 1994. Technique for calibration of meteorological radar using differential phase. *Electronics Letters* 30: 166–167.
46. Gorgucci, E., G. Scarchilli, and V. Chandrasekar. 1992. Calibration of radars using polarimetric techniques. *IEEE Transactions on Geoscience and Remote Sensing* 30: 853–858.
47. Gourley, J.J., A.J. Illingworth, and P. Tabary. 2009. Absolute calibration of radar reflectivity using redundancy of the polarization observations and implied constraints on drop shapes. *Journal of Atmospheric and Oceanic Technology* 26: 689–703.
48. Gourley, J.J., Y. Hong, Z.L. Flamig, J. Wang, H. Vergara, and E.N. Anagnostou. 2011. Hydrologic evaluation of rainfall estimates from radar, satellite, gauge, and combinations on Ft. Cobb Basin, Oklahoma. *Journal of Hydrometeorology* 12: 973–988.
49. Gu, J.-Y., A.V. Ryzhkov, P. Zhang, P. Neilley, M. Knight, B. Wolf, and D.-I. Lee. 2011. Polarimetric attenuation correction in heavy rain at C band. *Journal of Applied Meteorology and Climatology* 50: 39–58.
50. Hall, M.P.M., S.M. Cherry, J.W.F. Goddard, and G.R. Kennedy. 1980. Rain drop sizes and rainfall rate measured by dual-polarization radar. *Nature* 285: 195–198.
51. Harrington, J.Y., K. Sulia, and H. Morrison. 2013. A method for adaptive habit prediction in bulk microphysical models. Part I: Theoretical development. *Journal of the Atmospheric Sciences* 70: 349–364.
52. Heinselman, P.L., and A.V. Ryzhkov. 2006. Validation of polarimetric hail detection. *Weather and Forecasting* 21: 839–850.
53. Heymsfield, G.M., L. Tian, L. Li, M. McLinden, and J. Cervantes. 2013. Airborne radar observations of severe hailstorms Implications for future spaceborne radar. *Journal of Applied Meteorology and Climatology* 52: 1851–1867.
54. Hibbins, R.E., J.D. Shanklin, P.J. Epsy, M.J. Jarvis, D.M. Riggin, D.C. Fritts, and F.-J. Lübken. 2005. Seasonal variations in the horizontal wind structure from 0–100 km above Rothera station, Antarctica (67S, 68W). *Atmospheric Chemistry and Physics* 5: 2973–2980.
55. Hildebrand, P.H., and R.K. Moore. 1990. Meteorological radar observations from mobile platforms. In *Radar in Meteorology*, ed. D. Atlas, 287–314. Boston: American Meteorological Society.
56. Hildebrand, P.H., W.-C. Lee, C.A. Walther, C. Frush, M. Randall, E. Loew, R. Neitzel, R. Parsons, J. Testud, F. Baudin, and A. LeCornec. 1996. The ELDORA/ASTRAIA Airborne Doppler weather radar: high-resolution observations from TOGA COARE. *Bulletin of the American Meteorological Society* 77: 213–232.
57. Hocking, W.K. 1999. Temperatures using radar-meteor decay times. *Geophysical Research Letters* 26: 3297–3300. https://doi.org/10.1029/1999GL003618.
58. Hocking, W.K., B. Fuller, and B. Vandepeer. 1999. Real-time determination of meteor-related parameters utilizing digital technology. *Journal of Atmospheric and Solar—Terrestrial Physics* 63: 155–169.
59. Hubbert, J.C., V.N. Bringi, L.D. Carey, and S. Bolen. 1998. CSU-CHILL polarimetric radar measurements from a severe hail storm in eastern Colorado. *Journal of Applied Meteorology* 37: 749–775.

60. Hubbert, J.C., S.M. Ellis, M. Dixon, and G. Meymaris. 2010. Modeling, error analysis, and evaluation of dual- polarization variables obtained from simultaneous horizontal and vertical polarization transmit radar. Part I: Modeling and antenna errors. *Journal of Atmospheric and Oceanic Technology* 27: 1583–1598.
61. Hubbert, J.C., S.M. Ellis, M. Dixon, and G. Meymaris. 2010. Modeling, error analysis, and evaluation of dual-polarization variables obtained from simultaneous horizontal and vertical polarization transmit radar. Part II: Experimental data. *Journal of Atmospheric and Oceanic Technology* 27: 1599–1607.
62. Hubbert, J.C., S.M. Ellis, W.-Y. Chang, S. Rutledge, and M. Dixon. 2014. Modeling and interpretation of S-band ice crystal depolarization signatures from data obtained by simultaneously transmitting horizontally and vertically polarized fields. *Journal of Applied Meteorology and Climatology* 53: 1659–1677.
63. Illingworth, A., and T. Blackman. 2002. The need to represent raindrop size spectra as normalized gamma distributions for the interpretation of polarization radar observations. *Journal of Applied Meteorology* 41: 286–297.
64. Isom, B., R.D. Palmer, R. Kelley, J. Meier, D. Bodine, M. Yeary, B.L. Cheong, Y. Zhang, T.-Y. Yu, and M.I. Biggerstaff. 2013. The atmospheric imaging radar: Simultaneous volumetric observations using a phased array weather radar. *Journal of Atmospheric and Oceanic Technology* 30: 655–675.
65. Jameson, A.R. 1985. Microphysical interpretation of multiparameter radar measurements in rain. Part III: Interpretation and measurement of propagation differential phase shift between orthogonal linear polarizations. *Journal of the Atmospheric Sciences* 42: 607–614.
66. Jensen, A.A., and J.Y. Harrington. 2015. Modeling ice crystal aspect ratio evolution during riming: a single-particle growth model. *Journal of the Atmospheric Sciences* 72: 2569–2590.
67. Jiang, Z., M. Oue, J. Verlinde, E.E. Clothiaux, K. Aydin, G. Botta, and Y. Lu. 2017. What can we conclude about the real aspect ratios of ice particle aggregates from two-dimensional images? *Journal of Applied Meteorology and Climatology* 56: 725–734.
68. Jung, Y., G. Zhang, and M. Xue. 2008. Assimilation of simulated polarimetric radar data for a convective storm using the ensemble Kalman filter. Part I: Observation operators for reflectivity and polarimetric variables. *Monthly Weather Review* 136: 2228–2245.
69. Junyent, F., V. Chandrasekar, V.N. Bringi, S.A. Rutledge, P.C. Kennedy, D. Brunkow, J. George, and R. Bowie. 2015. Transformation of the CSU-CHILL radar facility to a dual-frequency, dual-polarization Doppler system. *Bulletin of the American Meteorological Society* 96: 975–996.
70. Kalesse, H., W. Szyrmer, S. Kneifel, P. Kollias, and E. Luke. 2016. Fingerprints of a riming event on cloud radar: Doppler spectra observations and modeling. *Atmospheric Chemistry and Physics* 16: 2997–3012. https://doi.org/10.5194/acp-16-2997-2016.
71. Kennedy, P.C., and S.A. Rutledge. 2011. S-band dual-polarization radar observations of winter storms. *Journal of Applied Meteorology and Climatology* 50: 844–858.
72. Kennedy, P.C., S.A. Rutledge, W.A. Petersen, and V.N. Bringi. 2001. Polarimetric radar observations of hail formation. *Journal of Applied Meteorology* 40: 1347–1366.
73. Kneifel, S., A. von Lerber, J. Tiira, D. Moisseev, P. Kollias, and J. Leinonen. 2015. Observed relations between snowfall microphysics and triple-frequency radar measurements. *Journal of Geophysical Research-Atmospheres* 120: 6034–6055. https://doi.org/10.1002/2015JD023156.
74. Kollias, P., B.A. Albrecht, R. Lhermitte, and A. Savtchenko. 2001. Radar observations of updrafts, downdrafts, and turbulence in fair-weather cumuli. *Journal of the Atmospheric Sciences* 58: 1750–1766.
75. Kollias, P., J. Remillard, E. Luke, and W. Szyrmer. 2011. Cloud radar Doppler spectra in drizzling stratiform clouds 1. Forward modeling and remote sensing applications. *Journal of Geophysical Research* 116: D13201.
76. Kosiba, K.A., J. Wurman, P. Markowski, Y. Richardson, P. Robinson, and J. Marquis. 2013. Genesis of the Goshen County, WY tornado on 05 June 2009 during VORTEX2. *Monthly Weather Review* 141: 1157–1181.

77. Kumjian, M.R. 2013. Principles and applications of dual-polarization weather radar. Part 1: Description of the polarimetric radar variables. *Journal of Operational Meteorology* 1 (19): 226–242.
78. Kumjian, M.R. 2013. Principles and applications of dual-polarization weather radar. Part 2: Warm and cold season applications. *Journal of Operational Meteorology* 1 (20): 243–264.
79. Kumjian, M.R. 2013. Principles and applications of dual-polarization weather radar. Part 3: Artifacts. *Journal of Operational Meteorology* 1 (21): 265–274.
80. Kumjian, M.R., and Z.J. Lebo. 2016. Large accumulations of small hail. In *28th Conference on Severe Local Storms*. Portland, OR: American Meteorological Society. 8A.4.
81. Kumjian, M.R., and K.A. Lombardo. 2017. Insights into the evolving microphysical and kinematic structure of northeastern U.S. winter storms from dual-polarization Doppler radar. *Monthly Weather Review* 145: 1033–1061.
82. Kumjian, M.R., and A.V. Ryzhkov. 2008. Polarimetric signatures in supercell thunderstorms. *Journal of Applied Meteorology and Climatology* 47: 1940–1961.
83. Kumjian, M.R., and A.V. Ryzhkov. 2009. Storm-relative helicity revealed from polarimetric radar measurements. *Journal of the Atmospheric Sciences* 66: 667–685.
84. Kumjian, M.R., and A.V. Ryzhkov. 2012. The impact of size sorting on the polarimetric radar variables. *Journal of the Atmospheric Sciences* 69: 2042–2060.
85. Kumjian, M.R., and A.D. Schenkman. 2014. The curious case of ice pellets in Middle Tennessee on 1 March 2014. *Journal of Operational Meteorology—Image of Note* 2 (17): 209–213.
86. Kumjian, M.R., J.C. Picca, S.M. Ganson, A.V. Ryzhkov, J. Krause, D.S. Zrnić, and A.P. Khain. 2010. Polarimetric radar characteristics of large hail. In *25th Conference on Severe Local Storms*, Denver, CO. 11.2. Boston: American Meteorological Society (Preprints).
87. Kumjian, M.R., S. Ganson, and A.V. Ryzhkov. 2012. Raindrop freezing in deep convective updrafts: a microphysical and polarimetric model. *Journal of the Atmospheric Sciences* 69: 3471–3490.
88. Kumjian, M.R., A.V. Ryzhkov, H.D. Reeves, and T.J. Schuur. 2013. A dual-polarization radar signature of hydrometeor refreezing in winter storms. *Journal of Applied Meteorology and Climatology* 52: 2549–2566.
89. Kumjian, M.R., A.P. Khain, N. BenMoshe, E. Ilotoviz, A.V. Ryzhkov, and V.T.J. Phillips. 2014. The anatomy and physics of Z_{DR} columns Investigating a polarimetric radar signature with a spectral bin microphysical model. *Journal of Applied Meteorology and Climatology* 53: 1820–1843.
90. Kumjian, M.R., S. Mishra, S.E. Giangrande, T. Toto, A.V. Ryzhkov, and A.R. Bansemer. 2016. Polarimetric radar and aircraft observations of saggy bright bands during MC3E. *Journal of Geophysical Research-Atmospheres* 121: 3584–3607.
91. Kuster, C.M., P.L. Heinselman, and T.J. Schuur. 2016. Rapid-update radar observations of downbursts occurring within an intense multicell thunderstorm on 14 June 2011. *Weather and Forecasting* 31: 827–851.
92. Lhermitte, R.M. 1987. A 94 GHz Doppler radar for cloud observations. *Journal of Atmospheric and Oceanic Technology* 4: 36–48.
93. Lhermitte, R.M. 1988. Observation of rain at vertical incidence with a 94 GHz Doppler radar: an insight on Mie scattering. *Geophysical Research Letters* 15: 1125–1128.
94. Lhermitte, R.M. 1990. Attenuation and scattering of millimeter wavelength radiation by clouds and precipitation. *Journal of Atmospheric and Oceanic Technology* 7: 464–479.
95. Li, X., and J.R. Mecikalski. 2012. Impact of the dual-polarization Doppler radar data on two convective storms with a warm-rain radar forward operator. *Monthly Weather Review* 140: 2147–2167.
96. Li, X., J.R. Mecikalski, and D. Posselt. 2017. An ice-phase microphysics forward model and preliminary results of polarimetric radar data assimilation. *Monthly Weather Review* 145: 683–708.

97. Lim, S., V. Chandrasekar, and V.N. Bringi. 2005. Hydrometeor classification system using dual-polarization radar measurements: model improvements and in situ verification. *IEEE Transactions on Geoscience and Remote Sensing* 43: 792–801.
98. Liu, H., and V. Chandrasekar. 2000. Classification of hydrometeors based on polarimetric radar measurements: development of fuzzy logic and neuro-fuzzy systems, and in situ verification. *Journal of Atmospheric and Oceanic Technology* 17: 140–164.
99. Loeffler, S.M., and M.R. Kumjian. 2016. Analysis of polarimetric radar signatures in tornadic non-supercellular storms. In *28th Conference on Severe Local Storms*, 12A.4. Boston: American Meteorological Society.
100. Loeffler, S.M., and M.R. Kumjian. 2016. Quantifying $Z_{DR} - K_{DP}$ separation in severe convective storms to assess tornadic potential. In *28th Conference on Severe Local Storms*, Poster 169. Boston: American Meteorological Society.
101. Lu, Y., E.E. Clothiaux, K. Aydin, G. Botta, and J. Verlinde. 2013. Modeling variability in dendritic ice crystal backscattering cross sections at millimeter wavelengths using a modified Rayleigh-Gans theory. *Journal of Quantitative Spectroscopy and Radiation Transfer* 131: 95–104.
102. Lu, Y., Z. Jiang, K. Aydin, J. Verlinde, E.E. Clothiaux, and G. Botta. 2016. A polarimetric scattering database for non-spherical ice particles at microwave wavelengths. *Atmospheric Measurement Techniques* 9: 5119–5134.
103. Luke, E., and P. Kollias. 2013. Separating cloud and drizzle radar moments during precipitation onset using Doppler spectra. *Journal of Atmospheric and Oceanic Technology* 30: 1656–1671.
104. Mahale, V.N., G. Zhang, and M. Xue. 2016. Characterization of the 14 June 2011 Norman, Oklahoma downburst through dual-polarization radar observations and hydrometeor classification. *Journal of Applied Meteorology and Climatology* 55: 2635–2655.
105. Maki, M., et al. 2012. Tokyo metropolitan area convection study for extreme weather resilient cities (TOMACS). Extended Abstracts. In *7th European Conference on Radar in Meteorology and Hydrology*, Toulouse, France.
106. Markowski, P.M., and Y.P. Richardson. 2010. *Mesoscale Meteorology in Midlatitudes*. 1st ed., 407 pp. Oxford: Wiley-Blackwell.
107. Matrosov, S.Y. 2017. Characteristic raindrop size retrievals from measurements of differences in vertical Doppler velocities at Ka- and W-band radar frequencies. *Journal of Atmospheric and Oceanic Technology* 34: 65–71.
108. McLaughlin, D., et al. 2009. Short-wavelength technology and the potential for distributed networks of small radar systems. *Bulletin of the American Meteorological Society* 90: 1797–1817.
109. Melnikov, V.M., and R.J. Doviak. 2009. Turbulence and wind shear in layers of large Doppler spectrum width in stratiform precipitation. *Journal of Atmospheric and Oceanic Technology* 26: 430–443.
110. Mie, G. 1908. Beiträge zur Optik trüber Medien, speziell kolloidaler Metallösungen. *Annals of Physics* 330: 377–445.
111. Moisseev, D.N., S. Lautaportti, J. Tyynela, and S. Lim. 2015. Dual-polarization radar signatures in snowstorms: role of snowflake aggregation. *Journal of Geophysical Research-Atmospheres* 120: 12644–12655.
112. Morrison, H., and J.A. Milbrandt. 2015. Parameterization of cloud microphysics based on the prediction of bulk ice particle properties. Part I: Scheme description and idealized tests. *Journal of the Atmospheric Sciences* 72: 287–311.
113. Morrison, H., J.A. Milbrandt, G.H. Bryan, K. Ikeda, S.A. Tessendorf, and G. Thompson. 2015. Parameterization of cloud microphysics based on the prediction of bulk ice particle properties. Part II: Case study and comparisons with observations and other schemes. *Journal of the Atmospheric Sciences* 72: 312–339.
114. Nolan, D.S. 2013. On the use of Doppler radar-derived wind fields to diagnose the secondary circulations of tornadoes. *Journal of the Atmospheric Sciences* 70: 1160–1171.

115. Ortega, K.L., J.M. Krause, and A.V. Ryzhkov. 2016. Polarimetric radar characteristics of melting hail. Part III: Validation of the algorithm for hail size discrimination. *Journal of Applied Meteorology and Climatology* 55: 829–848.
116. Oue, M., M.R. Kumjian, Y. Lu, J. Verlinde, K. Aydin, and E. Clothiaux. 2015. Linear depolarization ratios of columnar ice crystals in a deep precipitation system over the Arctic observed by zenith-pointing Ka-band Doppler radar. *Journal of Applied Meteorology and Climatology* 54: 1060–1068.
117. Park, H.S., A.V. Ryzhkov, D.S. Zrnić, and K.-E. Kim. 2009. The hydrometeor classification algorithm for the polarimetric WSR-88D: description and application to an MCS. *Weather and Forecasting* 24: 730–748.
118. Pazmany, A.L., J.B. Mead, H.B. Bluestein, J.C. Snyder, and J.B. Houser. 2013. A mobile, rapid-scanning X-band polarimetric (RaXPol) Doppler radar system. *Journal of Atmospheric and Oceanic Technology* 30: 1398–1413.
119. Picca, J., and A.V. Ryzhkov. 2012. A dual-wavelength polarimetric analysis of the 16 May 2010 Oklahoma City extreme hailstorm. *Monthly Weather Review* 140: 1385–1403.
120. Picca, J.C., D.M. Schultz, B.A. Colle, S. Ganetis, D.R. Novak, and M.J. Sienkiewicz. 2014. The value of dual-polarization radar in diagnosing the complex microphysical evolution of an intense snowband. *Bulletin of the American Meteorological Society* 95: 1825–1834.
121. Picca, J.C., D.M. Kingfield, and A.V. Ryzhkov. 2017. Utilizing a polarimetric size sorting signature to develop a convective nowcasting algorithm. In *18th Conference on Aviation, Range, and Aerospace Meteorology*, Seattle, WA. Boston: American Meteorological Society, 14.5.
122. Posselt, D.J., X. Li, S.A. Tushaus, and J.R. Mecikalski. 2015. Assimilation of dual-polarization radar observations in mixed- and ice-phase regions of convective storms: information content and forward model errors. *Monthly Weather Review* 143: 2611–2636.
123. Rasmussen, E.N., and D.O. Blanchard. 1998. A baseline climatology of sounding-derived supercell and tornado forecast parameters. *Weather and Forecasting* 13: 1146–1164.
124. Rasmussen, R.M., and A.J. Heymsfield. 1987. Melting and shedding of graupel and hail. Part I: Model physics. *Journal of the Atmospheric Sciences* 44: 2754–2763.
125. Richter, H., J. Peter, and S. Collis. 2014. Analysis of a destructive wind storm on 16 November 2008 in Brisbane, Australia. *Monthly Weather Review* 142: 3038–3060.
126. Rinehart, R.E. 2004. *Radar for Meteorologists*, 482 pp. Columbia, MO: Rinehart Publications.
127. Romine, G.S., D.W. Burgess, and R.B. Wilhelmson. 2008. A dual-polarization-radar-based assessment of the 8 May 2003 Oklahoma City area tornadic supercell. *Monthly Weather Review* 136: 2849–2870.
128. Ryzhkov, A.V. 2007. The impact of beam broadening on the quality of radar polarimetric data. *Journal of Atmospheric and Oceanic Technology* 24: 729–744.
129. Ryzhkov, A.V., T.J. Schuur, D.W. Burgess, and D.S. Zrnić. 2005. Polarimetric tornado detection. *Journal of Applied Meteorology* 44: 557–570.
130. Ryzhkov, A.V., S.E. Giangrande, V.M. Melnikov, and T.J. Schuur. 2005. Calibration issues of dual-polarization radar measurements. *Journal of Atmospheric and Oceanic Technology* 22: 1138–1155.
131. Ryzhkov, A.V., M. Pinsky, A. Pokrovsky, and A.P. Khain. 2011. Polarimetric radar observation operator for a cloud model with spectral microphysics. *Journal of Applied Meteorology and Climatology* 50: 873–894.
132. Ryzhkov, A.V., M.R. Kumjian, S.M. Ganson, and A.P. Khain. 2013. Polarimetric radar characteristics of melting hail. Part I: Theoretical simulations using spectral microphysical modeling. *Journal of Applied Meteorology and Climatology* 52: 2849–2870.
133. Ryzhkov, A.V., M.R. Kumjian, S.M. Ganson, and P. Zhang. 2013. Polarimetric radar characteristics of melting hail. Part II: Practical implications. *Journal of Applied Meteorology and Climatology* 52: 2871–2886.

134. Ryzhkov, A.V., M. Diederich, P. Zhang, and C. Simmer. 2014. Potential utilization of specific attenuation for rainfall estimation, mitigation of partial beam blockage, and radar networking. *Journal of Atmospheric and Oceanic Technology* 31: 599–619.
135. Ryzhkov, A.V., P. Zhang, H. Reeves, M. Kumjian, T. Tschallener, S. Trömel, and C. Simmer. 2016. Quasi-vertical profiles – a new way to look at polarimetric radar data. *Journal of Atmospheric and Oceanic Technology* 33: 551–562.
136. Sachidananda, M., and D.S. Zrnić. 1986. Differential propagation phase shift and rainfall rate estimation. *Radio Science* 21: 235–247.
137. Schenkman, A.D., M. Xue, A. Shapiro, K. Brewster, and J. Gao. 2011. Impact of CASA radar and Oklahoma Mesonet data assimilation on the analysis and prediction of tornadic mesovortices in an MCS. *Monthly Weather Review* 139: 3422–3445.
138. Schneebeli, M., N. Dawes, M. Lehning, and A. Berne. 2013. High-resolution vertical profiles of X-band polarimetric radar observables during snowfall in the Swiss Alps. *Journal of Applied Meteorology and Climatology* 52: 378–394.
139. Schrom, R.S., and M.R. Kumjian. 2016. Connecting microphysical processes in Colorado winter storms with vertical profiles of radar observations. *Journal of Applied Meteorology and Climatology* 55: 1771–1787.
140. Schrom, R.S., M.R. Kumjian, and Y. Lu. 2015. Polarimetric radar signatures of dendritic growth zones within Colorado winter storms. *Journal of Applied Meteorology and Climatology* 54: 2365–2388.
141. Schultz, C.J., et al. 2012. Dual-polarization tornadic debris signatures. Part I: Examples and utility in an operational setting. *Electronic Journal of Operational Meteorology* 13 (9): 120–137.
142. Seliga, T.A., and V.N. Bringi. 1976. Potential use of radar differential reflectivity measurements at orthogonal polarizations for measuring precipitation. *Journal of Applied Meteorology* 15: 69–76.
143. Seliga, T.A., and V.N. Bringi. 1978. Differential reflectivity and differential phase shift: applications in radar meteorology. *Radio Science* 13: 271–275.
144. Shapiro, A.M., C.K. Potvin, and J. Gao. 2009. Use of a vertical vorticity equation in variational dual-Doppler wind analysis. *Journal of Atmospheric and Oceanic Technology* 26: 2089–2106.
145. Silber, I., and C. Price. 2016. On the use of VLF narrowband measurements to study the lower ionosphere and the mesosphere-lower thermosphere. *Surveys in Geophysics*. https://doi.org/10.1007/s10712-016-9396-9.
146. Sinclair, V.A., D. Moisseev, and A. von Lerber. 2016. How dual-polarization radar observations can be used to verify model representation of secondary ice. *Journal of Geophysical Research-Atmospheres* 121: 10954–10970.
147. Skolnik, M.I. 2001. *Introduction to Radar Systems*, 772 pp. New York: McGraw Hill.
148. Snyder, J.C., H.B. Bluestein, G. Zhang, and S.J. Frasier. 2010. Attenuation correction and hydrometeor classification of high-resolution, X-band, dual-polarized mobile radar measurements in severe convective storms. *Journal of Atmospheric and Oceanic Technology* 27: 1979–2001.
149. Snyder, J.C., A.V. Ryzhkov, M.R. Kumjian, A.P. Khain, and J.C. Picca. 2015. A Z_{DR} column detection algorithm to examine convective storm updrafts. *Weather and Forecasting* 30: 1819–1844.
150. Spoden, P.J., R.A. Wolf, and L.R. Lemon. 2012. Operational uses of spectrum width. *Electronic Journal of Severe Storms Meteorology* 7 (2): 1–28.
151. Straka, J.M., and D.S. Zrnić. 1993. An algorithm to deduce hydrometeor types and contents from multiparameter radar data. In *26th Conference on Radar Meteorology*, Norman, OK, 513–516. Boston: American Meteorological Society (Preprints).

152. Sulia, K.J., and M.R. Kumjian. 2017. Simulated polarimetric fields of ice vapor growth using the adaptive habit model. Part I: Large-eddy simulations. *Monthly Weather Review* 145: 2281–2302.
153. Sulia, K.J., and M.R. Kumjian. 2017. Simulated polarimetric fields of ice vapor growth using the adaptive habit model. Part II: A case study from the FROST experiment. *Monthly Weather Review* 145: 2303–2323.
154. Testud, J., E. Le Bouar, E. Obligis, and M. Ali-Mehenni .2000. The rain profiling algorithm applied to polarimetric weather radar. *Journal of Atmospheric and Oceanic Technology* 17: 332–356.
155. Thompson, R.L., R. Edwards, J.A. Hart, K.L. Elmore, and P.M. Markowski. 2003. Close proximity soundings within supercell environments obtained from the Rapid Update Cycle. *Weather and Forecasting* 18: 1243–1261.
156. Thompson, R.L., C.M. Mead, and R. Edwards. 2007. Effective storm-relative helicity and bulk shear in supercell thunderstorm environments. *Weather and Forecasting* 22: 102–115.
157. Thompson, E.J., S.A. Rutledge, B. Dolan, V. Chandrasekar, and B.L. Cheong. 2014. A dual-polarization radar hydrometeor classification algorithm for winter precipitation. *Journal of Atmospheric and Oceanic Technology* 31: 1457–1481.
158. Tong, M., and M. Xue. 2005. Ensemble Kalman filter assimilation of Doppler radar data with a compressible nonhydrostatic model OSS experiments. *Monthly Weather Review* 133: 1789–1807.
159. Torres, S., Y.F. Dubel, and D.S. Zrnić. 2004. Design, implementation, and demonstration of a staggered PRT algorithm for the WSR-88D. *Journal of Atmospheric and Oceanic Technology* 21: 1389–1399.
160. Torres, S., R. Passarelli Jr., A. Siggia, and P. Karhunen. 2010. Alternating dual-pulse, dual-frequency techniques for range and velocity ambiguity mitigation on weather radars. *Journal of Atmospheric and Oceanic Technology* 27: 1461–1475.
161. Tridon, F., and A. Battaglia. 2015. Dual-frequency radar Doppler spectral retrieval of rain drop size distributions and entangled dynamics variables. *Journal of Geophysical Research-Atmospheres* 120: 5585–5601.
162. Trömel, S., M.R. Kumjian, A.V. Ryzhkov, C. Simmer, and M. Diederich. 2013. Backscatter differential phase—estimation and variability. *Journal of Applied Meteorology and Climatology* 52: 2529–2548.
163. Trömel, S., A.V. Ryzhkov, P. Zhang, and C. Simmer. 2014. Investigations of backscatter differential phase in the melting layer. *Journal of Applied Meteorology and Climatology* 53: 2344–2359.
164. Van Den Broeke, M.S., and S.T. Jauernic. 2014. Spatial and temporal characteristics of tornadic debris signatures. *Journal of Applied Meteorology and Climatology* 53: 2217–2231.
165. Van Den Broeke, M.S., D.M. Tobin, and M.R. Kumjian. 2016. Polarimetric radar observations of precipitation type and rate from the 2–3 March 2014 winter storm in Oklahoma and Arkansas. *Weather and Forecasting* 31: 1179–1196.
166. Van Lier-Walqui, M., A.M. Fridlind, A.S. Ackerman, S. Collis, J. Helmus, D.R. MacGorman, K. North, P. Kollias, and D.J. Posselt. 2016. On polarimetric radar signatures of deep convection for model evaluation: columns of specific differential phase observed during MC3E. *Monthly Weather Review* 144: 737–758.
167. Vincent, R.A., and I.M. Reid. 1983. HF Doppler measurements of mesospheric gravity waves momentum fluxes. *Journal of the Atmospheric Sciences* 40: 1321–1333.
168. Vivekanandan, J., D.S. Zrnić, S. Ellis, D. Oye, A.V. Ryzhkov, and J.M. Straka. 1999. Cloud microphysics retrieval using S-band dual-polarization radar measurements. *Bulletin of the American Meteorological Society* 80: 381–388.
169. Wakimoto, R.M., P. Stauffer, W.-C. Lee, N.T. Atkins, and J. Wurman. 2012. Finescale structure of the LaGrange, Wyoming, tornado during VORTEX2: GBVTD and photogrammetric analyses. *Monthly Weather Review* 140: 3397–3418.
170. Wurman, J. 1994. Vector winds from a single-transmitter bistatic dual-Doppler radar network. *Bulletin of the American Meteorological Society* 75: 983–994.

171. Wurman, J.M., and K.A. Kosiba. 2013. Finescale radar observations of tornado and mesocyclone structures. *Weather and Forecasting* 28: 1157–1174.
172. Wurman, J., and M. Randall. 2001. An inexpensive, mobile rapid-scan radar. In *30th Conference on Radar Meteorology*, Munich, Germany, P3.4. Boston: American Meteorological Society (Preprints).
173. Wurman, J., S. Heckman, and D. Boccippio. 1993. A bistatic multiple-Doppler radar network. *Journal of Applied Meteorology* 32: 1802–1814.
174. Wurman, J.M., J. Straka, E. Rasmussen, M. Randall, and A. Zahrai. 1997. Design and deployment of a portable, pencil-beam, pulsed, 3-cm Doppler radar. *Journal of Atmospheric and Oceanic Technology* 14: 1502–1512.
175. Yokota, S., H. Sako, M. Kunii, H. Yamauchi, and H. Niino. 2016. The tornadic supercell on the Kanto Plain on 6 May 2012: polarimetric radar and surface data assimilation with EnKF and ensemble-based sensitivity analysis. *Monthly Weather Review* 144: 3133–3157.
176. Zhang, G., R.J. Doviak, D.S. Zrnić, R.D. Palmer, L. Lei, and Y. Al-Rashid. 2011. Polarimetric phased-array radar for weather measurement: a planar or cylindrical configuration? *Journal of Atmospheric and Oceanic Technology* 28: 63–73.
177. Zrnić, D.S., and A.V. Ryzhkov. 1999. Polarimetry for weather surveillance radars. *Bulletin of the American Meteorological Society* 80: 389–406.
178. Zrnić, D.S., J.F. Kimpel, D.E. Forsyth, A. Shapiro, G. Crain, R. Ferek, J. Heimmer, W. Benner, T.J. McNellis, and R.J. Vogt. 2007. Agile-beam phased array radar for weather observations. *Bulletin of the American Meteorological Society* 88: 1753–1766.
179. Zrnić, D.S., R.J. Doviak, G. Zhang, and A.V. Ryzhkov. 2010. Bias in differential reflectivity due to cross coupling through the radiation patterns of polarimetric weather radars. *Journal of Atmospheric and Oceanic Technology* 27: 1624–1637.